Imaging Complex Structures of the Los Angeles Basin via Adjoint-State Travel-Time Tomography

Dan Wang[1], Shijie Hao[2] , Jing Chen[2] , Guojie Song[*1], and Ping Tong[2,3,4]

ABSTRACT

In this study, we present high-resolution seismic velocity models for the Los Angeles basin (LAB) and its adjacent area using adjoint-state travel-time tomography, fitting an extensive database of *P*- and *S*-wave travel times accumulated from 1980 to 2021. We select 151,193 first *P*-wave travel times and 149,997 first *S*-wave travel times from local earthquakes archived in the Southern California Earthquake Data Center to determine the velocity models, with earthquake locations updated at each iteration. With seismic stations spaced more than 3.5 km apart, our dataset has limited resolution in the uppermost 1–2 km. However, starting from three different initial models, our V_P models, which are optimally imaged between 3 and 15 km, show similar velocity heterogeneity and provide a better fit to the observed first travel-time data compared to the Community Velocity Model-Harvard 15.1.0 and Community Velocity Model-Southern California Earthquake Center 4.26. Our models provide a detailed delineation of the subsurface structure beneath the LAB, revealing significant velocity variations across active faults, a 10-km-thick sequence of sedimentary rocks within the basin, and a distinct basin margin marked by transitions from low to high-velocities. In addition, these models highlight basement structures with elevated V_P and V_S located at depths of 9 to 12 km and beyond. Specifically, beneath the northeastern part of the basin, the models demonstrate improved accuracy and reliability in reflecting the linear relationship between V_P and V_S in mafic rocks. The accurate delineation of the basin's structure provided by our models could also offer robust constraints for seismic response modeling and seismic hazard assessment in the region.

KEY POINTS

- Compressional and shear-wave velocity models for the Los Angeles region are obtained via adjoint-state travel-time tomography.
- The V_P models demonstrate improved performance in fitting four decades of first travel-time data archived by the Southern California Earthquake Data Center (SCEDC).
- The subsurface structure beneath the Los Angeles Basin (LAB) reveals basement structures, a 10 km thick sedimentary basin, and the basin margin.

Supplemental Material

INTRODUCTION

The Los Angeles basin (LAB) (Fig. 1a), located between the Peninsular Ranges (PR), the western Transverse Ranges, and the continental borderland in southern California, is a northwest-trending deep sedimentary basin, also known as an alluviated lowland (Yerkes *et al.*, 1965). It directly evolved from the subsidence between the right-oblique Whittier and Palos Verdes fault zones and the left-oblique Santa Monica fault (SMoF) system in the late Miocene (Wright, 1991). From a broader perspective, the basin's formation in the late Neogene was associated with the opening of the California Borderland and the rotational compression of the western Transverse Ranges (Crouch and Suppe, 1993; Ingersoll and Rumelhart, 1999; Tsutsumi *et al.*, 2001). The LAB and adjacent areas have undergone Pliocene and Quaternary shortening, evidenced by extensive folds and thrusts (Davis *et al.*, 1989). Examples of these thrusts include the Puente Hills Thrust and Upper Elysian Park Thrust (Fig. 1a), which exhibit nearly pure dip-slip motions and trend perpendicular to the plate boundary (Davis *et al.*, 1989).

Substantial research efforts (e.g., Persaud *et al.*, 2016; Muir *et al.*, 2021; Ghose *et al.*, 2023; Villa *et al.*, 2023) have focused

1. School of Sciences, Southwest Petroleum University, Chengdu, China; 2. Division of Mathematical Sciences, School of Physical and Mathematical Sciences, Nanyang Technological University, Singapore, Singapore, https://orcid.org/0000-0003-1594-3039 (SH); https://orcid.org/0000-0002-9083-3940 (JC); https://orcid.org/0000-0002-1937-3427 (PT); 3. Asian School of the Environment, Nanyang Technological University, Singapore, Singapore; 4. Earth Observatory of Singapore, Nanyang Technological University, Singapore, Singapore

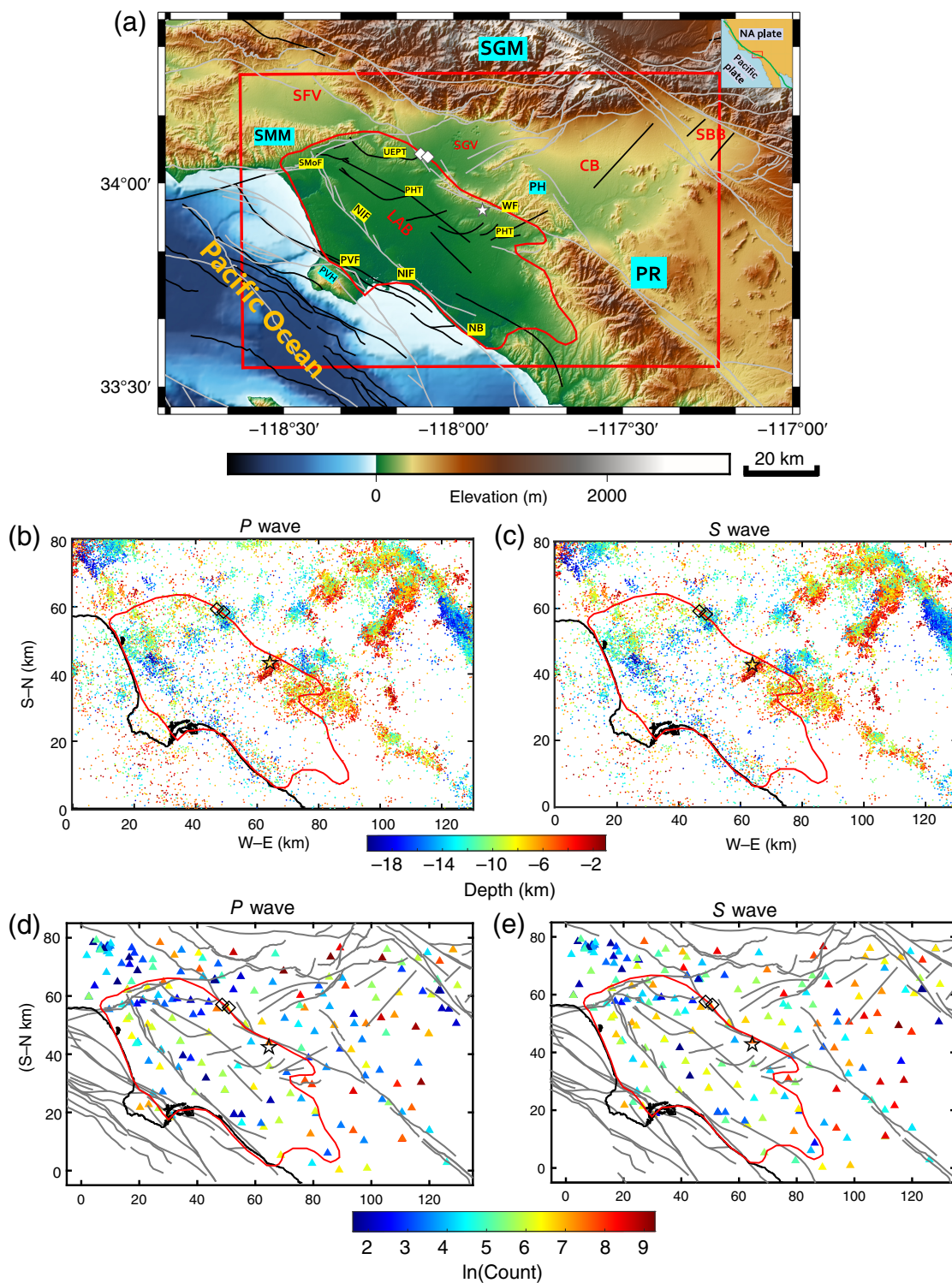*Corresponding author: cylsgj@126.com

Figure 1. (a) Tectonic setting and surface topography of the Los Angeles Basin (LAB) and adjacent areas. The gray curves denote fault traces, and the black curves denote blind faults (Marshall *et al.*, 2023). Fault abbreviation in the figures and main text include Santa Monica fault (SMoF), Whittier fault (WF), Puente Hills Thrust (PHT), Upper Elysian Park Thrust (UEPT), Newport–Inglewood fault (NIF), and Palos Verdes fault (PVF). The relief map highlights the distribution of valleys, basins, hills, and mountains, such as the San Gabriel Valley (SGV), San Fernando Valley (SFV), LAB, Chino Basin (CB), San Bernardino Basin (SBB), Newport Beach (NB), Santa Monica Mountains (SMM), San Gabriel Mountains (SGM), Palos Verdes Hills (PVH), Puente Hills (PH), and Peninsular Ranges (PR). The red box outlines the study area. (b,c) The spatial distribution of earthquakes with depths indexed by various colors. (d,e) The distribution of seismic stations is indicated by triangles where color represents the natural log of the count of selected travel times. The black curves in panels (b–e) represent the coastline near the LAB. The star represents the 2014 M_w 5.2 La Habra earthquake, and the diamonds represent the 1987 M_w 5.2 and 5.9 Whittier Narrows earthquakes. The color version of this figure is available only in the electronic edition.

on investigating basin amplification effects within the LAB. The amplified shaking effects, such as the constructive interference of direct waves with shallow basin-edge-generated surface waves and focusing by deep geologic structures, increase the seismic hazard of the LAB and adjacent regions (Gao *et al.*, 1996; Graves *et al.*, 1998; Davis *et al.*, 2000). The depth of a sedimentary basin affects the level of ground shaking during earthquakes. Using the *P* and *S* arrival times, Hauksson and Haase (1997) delineated the shape of the LAB, revealing depths from 8 to 12 km. Fuis *et al.* (2001), using refraction and reflection data, estimated the maximum depth of the LAB to be 8–9 km along the active source transect (line 1) of the Los Angeles Region Seismic Experiment. Chen *et al.* (2007) employed frequency-dependent phase-delay arrival times of *P* and *S* waves and a scattering-integral formulation of full 3D tomography to improve the Community Velocity Model 3.0 (CVM3.0) in the Los Angeles region, inferring a maximum basin depth of about 9 km. Previous studies (e.g., Yerkes *et al.*, 1965; Magistrale *et al.*, 1996; Qiu *et al.*, 2019) have generally suggested that the maximum depth of the LAB is about 10 km.

The level and duration of ground shaking are also influenced by the shape of the basin (Olsen *et al.*, 1995; Steidl *et al.*, 1995; Hauksson and Haase, 1997). At the eastern margin of the basin, Hauksson and Haase (1997) revealed a juxtaposition of high-velocity layers overlying low-velocity layers, indicating that the ongoing deformation of the hanging wall led to the closure of the LAB. Fuis *et al.* (2001) identified the Whittier Fault and the Sierra Madre Fault as steeply north-dipping buttress-like boundaries of the LAB and San Gabriel Valley (SGV), respectively. According to Bjorklund *et al.* (2002), the northwesterly alignment of high-V_P plutons may indicate the location of the northeastern LAB rift boundary, associated with the clockwise rotation of the western Transverse Ranges.

Given the complex geological setting and significant seismic activity in the region, understanding the seismic velocity structure of the LAB is crucial for assessing seismic hazards. Previous studies have also extensively investigated the seismic velocity structure of the LAB area. For example, Magistrale *et al.* (1996) developed a 3D V_P model of the LAB based on the depth to crystalline basement, depths to sedimentary horizons, uplift of sediments, and surface geology. This model demonstrated successful predictions of travel times and precise determination of the timing and amplitude of late-arriving waves. Hauksson and Haase (1997) revealed that three low-velocity areas within the LAB, namely Santa Monica, Long Beach, and the SGV, correlate with recent sediment deposition at 1 km depth. The high-V_P/V_S ratios near the surface align with the increased pore fluid pressures in the basin sediments (Hauksson and Haase, 1997).

Süss and Shaw (2003) developed a 3D V_P model of the LAB based on direct measurements from sonic logs obtained from oil wells and extracted from stacking velocities. The resulting model demonstrated that variations in sediment porosity and lithology are reflected in both horizontal and vertical changes in velocity and velocity gradient (Süss and Shaw, 2003). In recent years, several community velocity models, such as Community Velocity Model-Harvard 15.1.0 (CVM-H 15.1.0) and Community Velocity Model-Southern California Earthquake Center (SCEC) 4.26 (CVM-S 4.26), and other notable velocity models (Chen *et al.*, 2007; Tape *et al.*, 2009; Lee *et al.*, 2014; Shaw *et al.*, 2015) have been developed. These models are integrated and made accessible through the SCEC Unified Community Velocity Model Software (Small *et al.*, 2022). More recently, Muir *et al.* (2021) introduced a V_S model, revealing that the northeast hanging wall of the LAB is steeper than that depicted in the CVM-S model. This steepness facilitates high-amplifications of surface waves in the 4–6 s period band propagating within the basin. Jia and Clayton (2021) derived a shallow 3D shear-wave velocity model, illuminating that the Newport–Inglewood fault zone is a northwest–southeast-trending high-V_S belt.

In addition, receiver function, ambient noise tomography, and gravity modeling studies were carried out in and near the LAB using data from dense nodal arrays and the regional Southern California Seismic Network to produce high-resolution 3D seismic velocity and basin depth models for the sedimentary basins extending from the San Andreas fault to downtown Los Angeles (Liu *et al.*, 2018, 2021; Wang *et al.*, 2021; Ghose *et al.*, 2023; Li *et al.*, 2023; Villa *et al.*, 2023). High-resolution 3D seismic attenuation models using dense nodal arrays have identified scattering anomalies aligned with fault zones (Nardoni and Persaud, 2024). In general, these efforts provide enhanced local structure with detailed small-scale heterogeneities.

To further improve the resolution of the seismic velocity model for the LAB, leveraging additional seismic data through reliable tomography techniques is crucial. Over the past 40 yr, earthquakes in the LAB have generated abundant first *P*- and *S*-wave travel times, providing more data for tomographic inversions than before. Moreover, the adjoint-state travel-time tomography (ATT) method is a recently developed innovative approach that reformulates travel-time tomography as an eikonal equation-constrained optimization problem, solved by a ray-free adjoint-state method (Tong, 2021). This approach mitigates potential challenges associated with ray tracing in complex media and has higher efficiency compared to wave equation-based tomography methods. In this study, travel-time data of first-arriving *P* and *S* waves over the past 40 yr are carefully selected and inverted using the efficient and reliable ATT method within the study region (see Fig. 1a). The tomographic results are compared, interpreted, and discussed to provide new insight into the crustal structure of the LAB and its adjacent regions.

METHOD
Data
The study region, measuring 130 km × 80 km horizontally, encompasses the LAB, Chino basin (CB), SGV, San Fernando

TABLE 1
Improved 1D *P*-Wave Models for the Los Angeles Basin (LAB) Were Obtained by Referring to the Crust 1.0 Model (Laske *et al.*, 2013), the BBP 1D LAB 1D Model (Graves and Pitarka, 2010), and the Southern California Earthquake Center (SCEC) Modified Hadley–Kanamori (MHK) Model (Hutton *et al.*, 2010)

Depth (km)	5.0	[5.0,9.01)	[9.01, 19.66)	[19.66, Moho)	[Moho, 35.0]
Crust 1.0 (km/s)	4.00	6.00	6.50	7.10	8.09
Improved Crust 1.0 (km/s)	5.53	6.21	6.39	6.96	8.09
Depth (km)	5.0	[5.0,10.0)	[10.0, 15.5)	[15.5, Moho)	[Moho, 35.0]
MHK (km/s)	5.50	6.30	6.40	6.80	7.80
Improved MHK (km/s)	5.53	6.22	6.41	6.61	7.80
Depth (km)	5.0	[5.0,11.0)	[11.0, 21.0)	[21.0, Moho)	[Moho, 35.0]
BBP (km/s)	5.10	6.15	6.55	6.80	7.80
Improved BBP (km/s)	5.52	6.23	6.47	6.93	7.80

Three improved layered V_P models are then used to construct the initial 3D V_P models for the *P*-wave tomography and checkerboard test.

Valley, the eastern part of the Santa Monica Mountains (SMM), northwestern part of PR, the southern part of the San Gabriel Mountains (SGM), and Palos Verdes Hills (PVH) (Fig. 1a). We use handpicked first *P*-wave and *S*-wave arrival times archived in the Southern California Earthquake Data Center (Southern California Earthquake Data Center [SCEDC], 2013), where the standard deviation of picking travel-time errors is less than 0.1 s, to image the subsurface structures. The first *P*- and *S*-wave arrivals used in tomographic inversions are selected according to specific selection criteria to decluster earthquakes, ensure even coverage and the reliable use of seismic data. First, to mitigate the impact of uncertainties related to lower crust *P* and *S* velocities, Moho topography, and uppermost mantle *P* and *S* velocities, we exclude first arrivals refracted from the Moho discontinuity. Only earthquakes with a depth of less than 20 km and corresponding first arrivals at epicentral distances of less than 120 km are selected. Second, to reduce the clustering effect and ensure the uniformity of earthquake distribution, we divide the study region into small blocks of 0.5 km × 0.5 km × 0.5 km. Within each block, only the earthquake recorded by the maximum number of stations is retained, ensuring that the seismic travel-time data used within the same cube is of relatively high quality and reliability. Each selected station must record at least five first *P*- or *S*-wave arrivals to provide reliable constraints on the structure around the seismic station.

Based on these filtering rules, we obtain 151,193 first *P*-wave arrivals from 24,918 earthquakes (Fig. 1b) recorded by 218 stations (Fig. 1d), and 149,997 first *S*-wave arrivals from 22,701 earthquakes (Fig. 1c) recorded by 216 stations (Fig. 1e) between January 1980 and December 2021. Figure 1d,e shows the station distribution and the travel-time count for each station. As shown, the station distribution effectively covers the study region, with the exception of the offshore area. Although the travel-time counts in the northwestern part of the study region is generally lower than in the eastern part, the dense seismic station network in the northwest still provides sufficient constraints on the subsurface structures. The yearly counts of *P*- and *S*-wave arrival times are shown in Figure

S1a,b, respectively, demonstrating that most of the data were recorded from the early 2000s onward, with significant increases after 2010. However, *P*-wave travel times from the first 20 yr still account for about one-third of the total data, making a significant contribution to the V_P model. Although *S*-wave travel times from this period represent a smaller portion of the total, they still provide valuable constraints for the V_S model. Moreover, we observe that seismicity and selected earthquakes densely cover the study area from near the surface to a depth of 18 km (Fig. S1c,d). In general, the distributions of *P*- and *S*-wave data show dense coverage, providing sufficient constraints on the subsurface structure beneath the LAB. In addition, Figure S1e,f shows the spatial distributions of *P*- and *S*-wave travel-time kernels at six different depths, which can be considered equivalently as ray coverage or illumination. The illumination for both *P*- and *S*-wave data is highest onshore at depths of 3–15 km but decreases significantly below 15 km depth. Considering that the average minimum spacing of seismic stations is greater than 3.5 km, the resolution of our dataset is limited for very shallow structures, particularly at depths of 1–2 km. Consequently, our models are optimally imaged at depths from 3 to 15 km.

Initial V_P models

The construction of an appropriate initial velocity model that is representative of the large-scale geological features is a fundamental step in tomographic inversions. To mitigate the impact or bias caused by a single initial model on the final tomographic model, we construct three different initial velocity models. Layered V_P models, consisting of five layers, are constructed by referencing existing models such as the global Crust 1.0 model (Laske *et al.*, 2013), the LAB 1D model used in SCEC Broadband Platform (BBP) (Graves and Pitarka, 2010), and the SCEC-modified Hadley–Kanamori (MHK) model (Hutton *et al.*, 2010). A total of 201,448 preselection *P*-wave first travel times were used to improve the 1D layered V_P models. The outcomes of three refined 1D V_P models are presented in Table 1.

For the Crust 1.0 model, after 40 iterations, the refined 1D model stabilizes, and the root mean square (rms) reduces from 0.7151 to 0.2143 s. For the SCEC MHK model, the 1D model stabilizes after four iterations, with the rms decreasing from 0.2170 to 0.2138 s. The improved model, based on the BBP 1D model, stabilizes after 12 iterations, and the rms reduces from 0.2842 to 0.2140 s. The similarity among the three final rms values could serve as an indicator of the convergence achieved in the 1D V_P inversions. The reduction of the rms value for the Crust 1.0 model is significantly greater than that in the MHK and BBP models, likely because the MHK and BBP models are localized to the study area, whereas the Crust 1.0 model was built as a global crustal model. The undulating Moho discontinuity (Li et al., 2021) is incorporated into the three refined 1D velocity models to obtain three 3D initial V_P models for tomographic inversions. Note that a Gaussian function is applied to smooth the velocity discontinuity across each layer. The derived three smoothly varying 3D V_P models, based on the Crust 1.0 (Laske et al., 2013), the BBP 1D (Graves and Pitarka, 2010), and MHK (Hutton et al., 2010), respectively, are used as the initial models for the subsequent P-wave tomographic inversions. Specifically, the 3D V_P model created on the Crust 1.0 V_P model (Laske et al., 2013) is also used as the initial model for P-wave checkerboard resolution test. The construction of an initial model for S-wave checkerboard resolution test follows a similar workflow, referencing the Crust 1.0 V_S model (Laske et al., 2013).

Methodology

In our study, we employ the ATT (Tong, 2021) to develop crustal velocity models for the LAB and its adjacent regions. This method reformulates seismic travel-time tomography as an eikonal equation-based optimization problem solved by the efficient ray-free adjoint-state method. From the source x_s to any point $x = (x, y, z)$ inside the computational domain, the travel time $T_n(x)$ of the first P or S arrival is modeled by an eikonal equation. The subscript n represents the nth earthquake. The objective function $\chi(s(x))$ measures the discrepancy between the calculated travel time $T_n(x)$ and the observed traveltime $T_n^o(x)$, shown as

$$\chi(s(x)) = \sum_{n=1}^{N} \sum_{m=1}^{M} \frac{\omega_{n,m}}{2} \left[T_n\left(x_{r,m}\right) - T_n^o\left(x_{r,m}\right) \right]^2, \quad (1)$$

in which $\omega_{n,m}$ is the weight assigned to a specific observation. The subscript m denotes the mth station. M and N are the total number of seismic stations and earthquakes, respectively. $x_{r,m}$ represents the location of the mth seismic station deployed at or near the Earth's surface. The derivative of the objective function with respect to the slowness can be expressed by

$$\delta\chi(s(x)) = \sum_{n=1}^{N} \int_{\Omega} P_n(x)s(x)\delta s(x)dx = \int_{\Omega} K_s(x) \frac{\delta s(x)}{s(x)} dx, \quad (2)$$

in which the adjoint field $P_n(x)$ satisfies the following equation:

$$\nabla \cdot [P_n(x)(-\nabla T_n(x))] = \sum_{m=1}^{M} \omega_{n,m}[T_n(x) - T_n^o(x_{r,m})]\delta(x - x_{r,m}), \quad (3)$$

with a homogeneous boundary condition $P_n(x) = 0$, $x \in \partial\Omega$. The ∇ symbol is the gradient operator. The $\cdot$ symbol is the dot product. $\delta(x - x_{r,m})$ is the Dirac delta function. $K_s(x)$, the sum of the products of the adjoint field $P_n(x)$ and the square of the slowness $s^2(x)$, represents an event sensitivity kernel. The adjoint field $P_n(x)$ can be directly determined by solving the adjoint equation (3) and eikonal equation. This implies that the optimization problem (1) can be efficiently solved using accurate numerical methods, eliminating the need for ray tracing.

In the calculation process, we initially solve the eikonal equation and adjoint equation on a fine grid measuring 0.25 km × 0.25 km × 0.4 km, using the fast-sweeping method to obtain the travel-time field $T_n(x)$ and adjoint field $P_n(x)$ (Zhao, 2004; Leung and Qian, 2006), respectively. The computational domain extends to a depth of 35 km below sea level and 4 km above sea level, incorporating the elevation of all stations. Given the significantly higher number of earthquakes compared to stations, we optimize computational efficiency by designating selected earthquakes as virtual receivers and seismic stations as virtual sources. The virtual sources (seismic stations) are independent, enabling parallel processing for forward modeling. Subsequently, we compute the sensitivity kernel $K_n(x)$ using the adjoint field $P_n(x)$ and slowness $s(x)$. To discretize the relative slowness perturbation $\delta s(x)/s(x)$, we employ trilinear interpolation $B_{l,h}(x)$ on regular inversion grids, which are chosen based on the outcomes of a series of checkerboard resolution tests. $\delta s(x)$ is used to measure the disparity between a new model and the current iterative model. Using a step-size-controlled gradient descent algorithm to address the optimization problem (Tong, 2021), we iteratively obtain the optimal average of five velocity models from multiple grids (Tong et al., 2019).

Given that the discrepancy measured by the objective function is a combined effect of velocity heterogeneities and earthquake locations, we employ an eikonal equation-based earthquake location method (Tong, 2021) to update earthquake locations, alternating between inverting for seismic velocity and earthquake locations throughout each iteration in our workflow (Fig. S2, available in the supplemental material to this article). Utilizing the reciprocity theorem, the objective function of locating an earthquake is expressed as

$$\chi(x_{s,n},\tau_n) = \sum_{m=1}^{M} \frac{\omega_{m,n}}{2} [T_m(x_{s,n}) - (\tau_{m,n}^o - \tau_n)]^2, \quad (4)$$

in which τ_n is the origin time of the earthquake; and $\tau_{m,n}^o$ is the observed arrival time at a receiver location. The gradient of the objective function $\nabla\chi(x_{s,n},\tau_n)$ and the optimal origin time $\hat{\tau}_n$ are derived as

$$\nabla \chi(\mathbf{x}_{s,n}, \tau_n) = \sum_{m=1}^{M} \omega_{m,n} [T_m(\mathbf{x}_{s,n}) - (\tau_{m,n}^o - \hat{\tau}_n)] \cdot \nabla T_m(\mathbf{x}_{s,n}), \quad (5)$$

$$\hat{\tau}_n = \frac{\sum_{m=1}^{M} \omega_{m,n} (\tau_{m,n}^o - T_m(\mathbf{x}_{s,n}))}{\sum_{m=1}^{M} \omega_{m,n}}. \quad (6)$$

The step-size-controlled gradient descent algorithm (Tong, 2021) is adopted to determine the optimal earthquake location $\mathbf{x}_{s,n}$ in an iterative manner, eliminating the need for ray tracing. After the tomographic inversion, the average horizontal and vertical shifts of the final relocated earthquakes from the initial catalog are ~0.55 and 0.54 km, respectively.

Checkboard resolution tests

Before performing seismic tomographic inversions, we need to conduct checkerboard resolution tests to verify the reliability of the selected inversion parameters and the resolving ability of the chosen P- and S-wave data. The synthesized travel-time data are computed in a target velocity model using the fast-sweeping method (Zhao, 2004; Leung and Qian, 2006) and the source-station locations of the selected P- and S-wave data. Travel-time picking errors were modeled by adding Gaussian noise to the synthetic travel times. The mean and standard deviation of the Gaussian noise are 0.0 and 0.05 s, respectively.

To assess the resolution ability of the selected P-wave data, we design three target models with different sizes of anomalies. The three target velocity models, m_{c1}, m_{c2}, and m_{c3}, are built by imposing alternating high- and low-velocity anomalies, Δm_1, Δm_2, and Δm_3, onto the initial model m_0. The velocity anomalies have multiscale features constructed by sine functions, which can be expressed as

$$\Delta m_1 = \frac{m_{c1} - m_0}{m_0}$$
$$= \begin{cases} 8\% \sin\left(\frac{\pi x}{25}\right) \sin\left(\frac{\pi y}{25}\right) \sin\left(\pi \frac{\sqrt{25+8z}-5}{4}\right), & z > -7.0 \\ 8\% \sin\left(\frac{\pi x}{33.33}\right) \sin\left(\frac{\pi y}{37.5}\right) \sin\left(\pi \frac{\sqrt{25+8z}-5}{4}\right), & z < -7.0 \end{cases}, \quad (7)$$

$$\Delta m_2 = \frac{m_{c2} - m_0}{m_0}$$
$$= \begin{cases} 8\% \sin\left(\frac{\pi x}{20}\right) \sin\left(\frac{\pi y}{20}\right) \sin\left(\pi \frac{\sqrt{25+8z}-5}{4}\right), & z > -7.0 \\ 8\% \sin\left(\frac{\pi x}{26.67}\right) \sin\left(\frac{\pi y}{30}\right) \sin\left(\pi \frac{\sqrt{25+8z}-5}{4}\right), & z < -7.0 \end{cases}, \quad (8)$$

$$\Delta m_3 = \frac{m_{c3} - m_0}{m_0}$$
$$= \begin{cases} 8\% \sin\left(\frac{\pi x}{15}\right) \sin\left(\frac{\pi y}{15}\right) \sin\left(\pi \frac{\sqrt{25+8z}-5}{4}\right), & z > -7.0 \\ 8\% \sin\left(\frac{\pi x}{20}\right) \sin\left(\frac{\pi y}{22.5}\right) \sin\left(\pi \frac{\sqrt{25+8z}-5}{4}\right), & z < -7.0 \end{cases}, \quad (9)$$

in which 8% is the maximum amplitude of the relative velocity perturbation. As shown in equations (7)–(9), the sizes of the horizontal velocity anomalies in the x or y direction vary among the three models. At shallow depths (<7 km), the horizontal anomaly sizes of the three models are 25, 20, and 15 km, respectively. For all models below 7 km depth, the horizontal anomaly sizes increase by 33.3% in the x-direction (latitude) and 50.0% in the y-direction (longitude) compared to those at shallower depths. This adjustment is designed to honor the fact that seismic data have reduced resolution as depth increases. For example, from the uppermost crust down to a depth of 35 km, the size of the velocity anomaly Δm_2 changes from $20 \times 20 \times 5$ km³ to $26.67 \times 30 \times 17.46$ km³. The checker size in a checkerboard resolution test does not need to be square and can be arbitrary. For demonstration purposes, and considering that data resolution decreases with depth, we adjusted the size of the checkers below 7 km.

The inversion grids used in the three checkerboard tests are shown in Figure S3, with horizontal spacing of about 12.5, 10.0, and 7.5 km, respectively, to ensure that one wavelength, containing two velocity anomalies, is captured by five nodes of a single grid. As described by Tong et al. (2019), the multiple-grid model parameterization outperforms the traditional single grid in capturing heterogeneous subsurface velocity structures. Hence, we employ five sets of regular inversion grids (Fig. S3) to discretize the velocity perturbation, as previous studies have done (e.g., Tong et al., 2019, 2021; Tong, 2021; Qi and Tong, 2022; Wu, Li, et al., 2022). The five sets of inversion grids are laterally and vertically shifted by 0.2 times the spacing of one regular grid. The output model at each iteration is determined by taking the average of the five velocity models generated on the five sets of inversion grids. Moreover, the five sets of relatively sparse inversion grids compared to the forward grid act as smoothing regularization during the execution of the gradient descent method.

The results of the first and second P-wave checkerboard resolution tests, using the ATT method, suggest that the high- and low-velocity anomalies at scales of 20 km and above are recovered beneath the LAB and its eastern region (Fig. S4a,b). However, in the third checkerboard test (Fig. S4c), the recovery of velocity anomalies at a scale of 15 km is less satisfactory, such as in areas beneath the Newport–Inglewood fault and the PVH at depths of 2–5 km (Fig. S4c). Therefore, the parameters used in the second checkerboard test, which are designed to resolve horizontal velocity anomalies at scales of 20 km and above, are considered appropriate for subsequent tomographic inversions. In addition, the maximum amplitude of the recovered anomalies (Fig. S4b, ~6.5%) is about 18.75% smaller than the 8% of the target model (Fig. S4d), primarily due to the introduced picking errors. The model is not as well imaged below 15 km, primarily due to insufficient data coverage at these deeper crustal levels.

To evaluate the performance of the integrated workflow of eikonal equation-based earthquake location and velocity inversion with the chosen seismic data, we conduct an integrated

P-wave checkerboard resolution test that includes both earthquake relocation and velocity inversion. All settings are the same as in the second *P*-wave checkboard test, but the earthquake locations and origin times are deliberately perturbed by sine and cosine functions, as shown in equations (10) and (11). $e(\mathrm{x})$ and $e(T)$ represent the perturbed errors of earthquake locations and origin times, respectively. x_i and $\mathrm{x}_i^{\mathrm{used}}$ are the earthquake locations from the earthquake catalog and the perturbed earthquake locations, respectively. Similarly, T_i^{used} and T_i represent the perturbed travel times and those computed in the target model of the second checkboard test. From equation (10), the spatial errors are within 2 km in the *x*-direction, 2 km in the *y*-direction, and 4 km in the *z*-direction. In addition, based on equation (11), the temporal error is within 0.4 s. These spatial and temporal errors are introduced to mimic true catalog errors or hypocenter uncertainties when calculating the synthetic travel-time data:

$$e(\mathrm{x}) = \mathrm{x}_i^{\mathrm{used}} - \mathrm{x}_i$$
$$= \left[2\sin\left(\frac{2\pi i}{61}\right)\cos\left(\frac{2\pi i}{101}\right), 2\sin\left(\frac{2\pi i}{61}\right)\sin\left(\frac{2\pi i}{101}\right), 4\cos\left(\frac{2\pi i}{103}\right) \right],$$
$$(i = 1,\ldots,24{,}925). \tag{10}$$

$$e(T) = T_i^{\mathrm{used}} - T_i = 0.4\cos\left(\frac{2\pi i}{107}\right), (i = 1,\ldots,151{,}432). \tag{11}$$

The results of the integrated *P*-wave checkerboard resolution test at six representative depths (Fig. 2a–f) suggest that, compared with those in Figure S4d, the high- and low-velocity anomalies, along with their high-gradients beneath the land, particularly in the LAB, can be effectively recovered using the selected parameters, spatial distributions of the *P*-wave seismic data, and the integrated workflow. However, the velocity anomalies offshore are less well resolved due to the lack of offshore seismic stations. All these tests suggest that the chosen inversion parameters, *P*-wave travel times, and workflow can be reliably adopted for the subsequent tomographic inversion to construct a V_P model for the LAB and its eastern region, achieving horizontal and vertical resolutions of about 20 and 5 km, respectively.

To evaluate the resolving ability of the chosen *S*-wave data, a similar integrated checkerboard resolution test is performed. The parameter settings, velocity perturbations in the initial V_S model, and workflow is consistent with those in the integrated *P*-wave checkboard test. Compared with Figure S4d, the results of the *S*-wave checkerboard test (Fig. 2g–l) show that the positive and negative velocity anomalies, along with their high-gradient, are recovered within the LAB and its eastern region, while the offshore area is less well resolved. Consequently, the selected inversion parameters, *S*-wave travel times, and workflow can also be reliably adopted for subsequent real tomographic inversion to build a V_S model for the LAB and its eastern region, achieving horizontal and vertical resolutions of about 20 and 5 km, respectively.
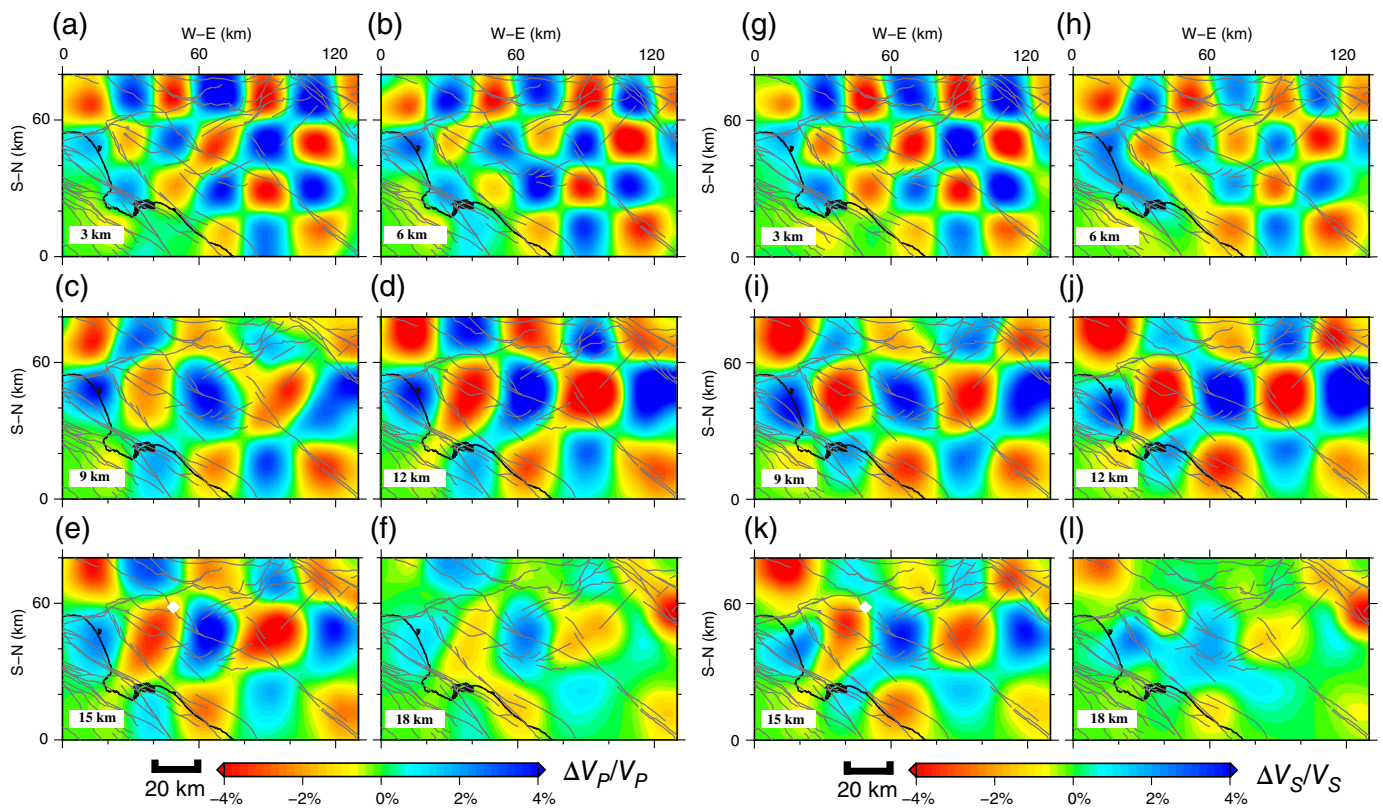
TOMOGRAPHIC RESULTS
V_P model
Adopting the inversion parameters from the *P*-wave checkerboard tests above, we invert the observed first *P*-wave arrival times to generate crustal V_P models, gridded at 0.25 km × 0.25 km × 0.4 km, starting from three initial V_P models. The iterative reduction of the objective function for each of the three models exhibits a similar convergence trend (Fig. S5a), and stability is achieved after 20 iterations. For instance, when choosing the improved MHK model as the initial model, the objective function value (the sum of square of travel-time misfits) reduces from 4673 to 1960 s^2. Figures 3 illustrates the horizontal V_P maps extracted from previous V_P models, such as CVM-H 15.1 (Shaw *et al.*, 2015) and CVM-S 4.26 (Lee *et al.*, 2014), and the three tomographic V_P models obtained in this study. The relative velocity perturbation of the final tomographic V_P model, using the improved MHK model as the initial model, is also included in Figure 3, reflecting that the perturbations are purely contributed by the selected travel-time data.

To quantitatively compare the five V_P models, we conduct a forward calculation assessment using the remaining 46,974 *P*-wave first-arrival travel times after selection in the Data section. Corresponding earthquake locations are updated according to the accurate waveform-relocated earthquake catalog of southern California (Hauksson *et al.*, 2012). The forward calculation is performed using the fast-sweeping method to solve the eikonal equation (Zhao, 2004; Leung and Qian, 2006). Detailed quantitative assessments of the five models, represented by the rms residuals between synthetic and observed travel-time data, are provided in Table 2. The results in Table 2 indicate that the three tomographic V_P models obtained in this study fit the observed first *P*-wave travel-time data better than the two published models. The rms values for these three tomographic V_P models are comparable, ranging from one-third to one-half of those for the two published V_P models. In addition, there is little difference among the tomographic results (Fig. 3g–o,y–gg) obtained from the three different initial V_P models, suggesting that the dense distribution of earthquakes and seismic stations makes the variations among the three models insignificant. For this reason, we consider our tomographic results reliable. Henceforth, the mentioned V_P model refers to the final tomographic model using the improved SCEC MHK (Hutton *et al.*, 2010) model as the initial model, that is, the final 3D tomographic MHK V_P model.

V_S model and V_P/V_S model
The initial 3D V_S model is obtained by dividing the final 3D tomographic MHK V_P model by a constant ratio. Previous studies in the LAB area have consistently demonstrated elevated V_P/V_S ratios (Hauksson and Haase, 1997, their fig. 4; Hauksson, 2000, their plate 2). To determine an appropriate constant V_P/V_S ratio, we conduct a test by computing the objective function in various V_S models generated by scaling

Figure 2. Results of checkerboard resolution tests for (a–f) *P* wave and (g–l) *S* wave obtained through iterative and alternative updates of velocity structure and earthquake locations. The six panels to the left make the *P*-wave model, and the six panels to the right the *S*-wave model. Map views are presented at depths of 3, 6, 9, 12, 15, and 18 km. The color scale for relative velocity perturbations is shown at the bottom. The gray curves represent fault traces and blind faults (Marshall *et al.*, 2023). The color version of this figure is available only in the electronic edition.

the final V_P model with a V_P/V_S ratio ranging from 1.720 to 1.780 at an interval of 0.002. The curve of the objective function values with respect to the V_P/V_S ratio resembles a quasi-quadratic function (Fig. 4), reaching its minimum when the V_P/V_S ratio equals 1.760. Subsequently, the initial 3D V_S model is obtained by dividing the V_P in the final 3D V_P MHK model by 1.760. The current procedure has a significant advantage: the objective function of *S*-wave tomography generated from the initial V_S model for the *S*-wave checkerboard test is 23,144 s², much higher than that of the currently constructed initial V_S model, which is 15,707 s².

The tomographic V_S model is obtained iteratively. After 20 iterations, the V_S model becomes stable (Fig. S5b). The objective function value is reduced from 15,707 to 8,380 s², representing a reduction of 46.6%, similar to that observed in the *P*-wave tomographic inversion. Potential factors contributing to the remaining misfit may include errors in travel-time picks, unresolvable small-scale heterogeneities, seismic anisotropy, and others. Figure 5 demonstrates the horizontal V_S views, extracted from CVM-H 15.1 (Shaw *et al.*, 2015), CVM-S 4.26 (Lee *et al.*, 2014), and our final tomographic V_S model.

The final V_P/V_S model of this study is generated by computing the ratio of the tomographic MHK V_P to the final V_S model. Figure 6 also shows the horizontal V_P/V_S views provided by CVM-H 15.1 (Shaw *et al.*, 2015), CVM-S 4.26 (Lee *et al.*, 2014), and this study. Figures 7 and 8 show the vertical views of V_P, V_S, and V_P/V_S models provided by CVM-H 15.1 (Shaw *et al.*, 2015), CVM-S 4.26 (Lee *et al.*, 2014), and this study. To

visually depict the tomographic results, we present the 3D geometries of V_P and V_P/V_S anomalies in Figure 9a–d, respectively.

DISCUSSION

Our V_P, V_S, and V_P/V_S models exhibit significant heterogeneities and share many features with previous studies (e.g., Haukason and Haase, 1997; Haukasson, 2000; Süss and Shaw, 2003; Chen *et al.*, 2007; Lee *et al.*, 2014; Shaw *et al.*, 2015). Specifically, comparisons (Figs. 3a–o,s–gg, 5a–r, 6a–r, and 8a–i) among CVM-H 15.1.0, CVM-S 4.26, and our V_P, V_S, and V_P/V_S models of this study show that the locations of large-scale low- and high-velocity patterns in the upper crust are consistent. The significant variations in V_P, V_S, and V_P/V_S illuminate the different rock types beneath the study region.

Notably, some distinct features obtained in the present study, marked by the dashed circles in the figures, differ from those in CVM-H 15.1.0 and CVM-S 4.26 models. In the following sections, we discuss the observed V_P, V_S, and V_P/V_S patterns, the reliability for which is verified by the checkerboard resolution
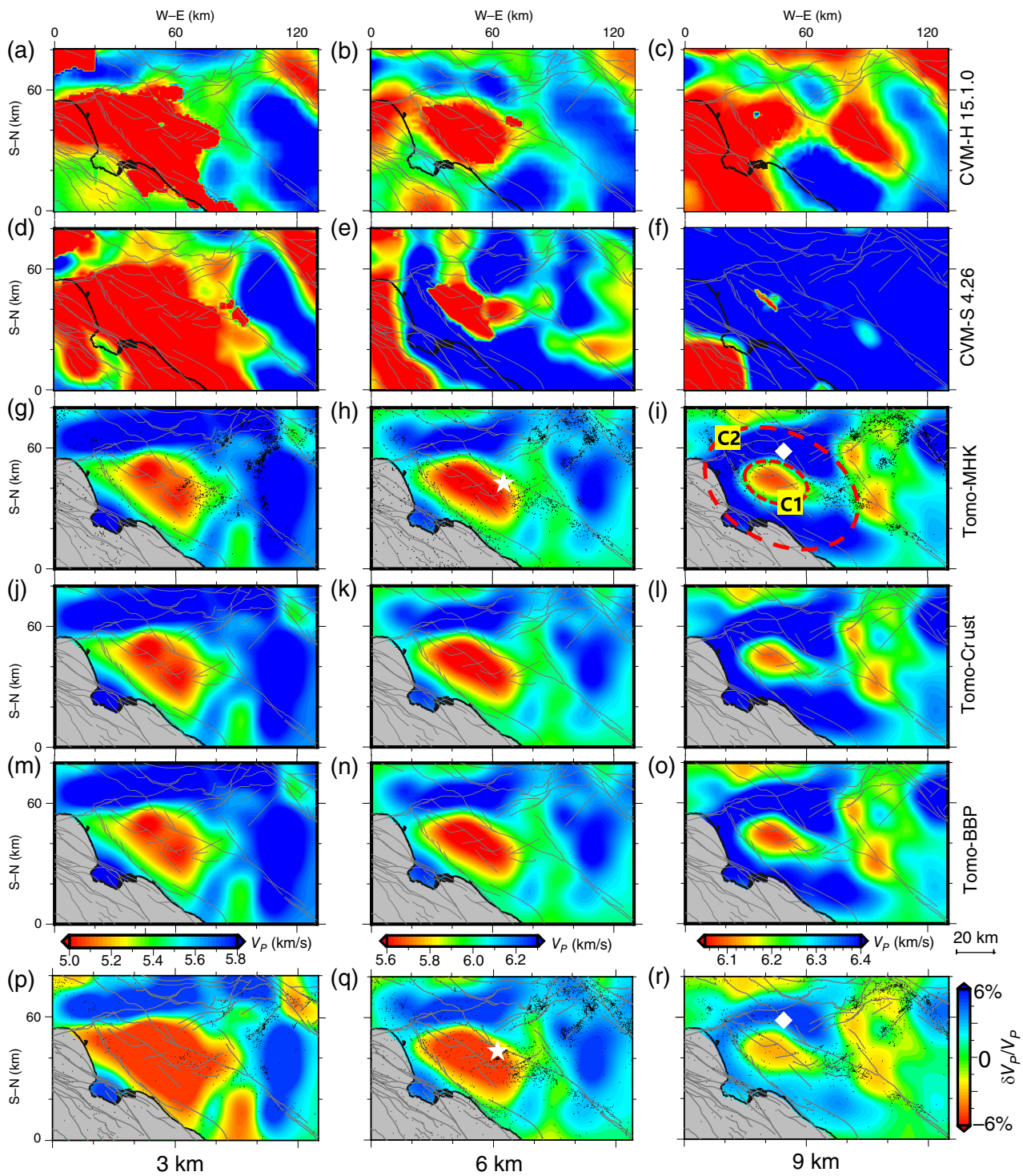
Figure 3. Comparison of V_P models in map views among (a–c,s–u) Community Velocity Model-Harvard 15.1 (CVM-H 15.1) (Shaw *et al.*, 2015), (d–f,v–x) Community Velocity Model-Southern California Earthquake Center 4.26 (CVM-S 4.26) (Lee *et al.*, 2014), and the models generated from (g–i,y–aa) modified Hadley–Kanamori (MHK) model (Hutton *et al.*, 2010), (j–l,bb–dd) Crust 1.0 model (Laske *et al.*, 2013), and (m–o,ee–gg) BBP model (Graves and Pitarka, 2010). The relative velocity perturbation of the final *P*-wave velocity model with respect to the initial 3D MHK model is shown in (p–r,hh–jj). Velocity models are displayed at representative depths of 3, 6, 9, 12, 15, and 18 km. Each color scale inset at the bottom shows the absolute velocity at the same depth. The color scales for V_P perturbation are shown on the right. Notable differences among various models are indicated by dashed circles and numbered. The gray curves represent fault traces and blind faults (Marshall *et al.*, 2023). The black dots in the final velocity model using the MHK model as the initial model denote earthquakes since 1980 that occurred within 0.5 km of the map view. The star in panels (h) and (q) represent the 2014 M_w 5.2 La Habra earthquake. The diamonds in panels (i,r) and (z,ii) mark the 1987 M_w 5.2 Whittier Narrows aftershock and M_w 5.9 mainshock, respectively. The black curves represent the coastline near the LAB. H1–H3 denote high-velocity rocks. L1 represents a low-velocity anomaly. The color version of this figure is available only in the electronic edition. (*Continued*)
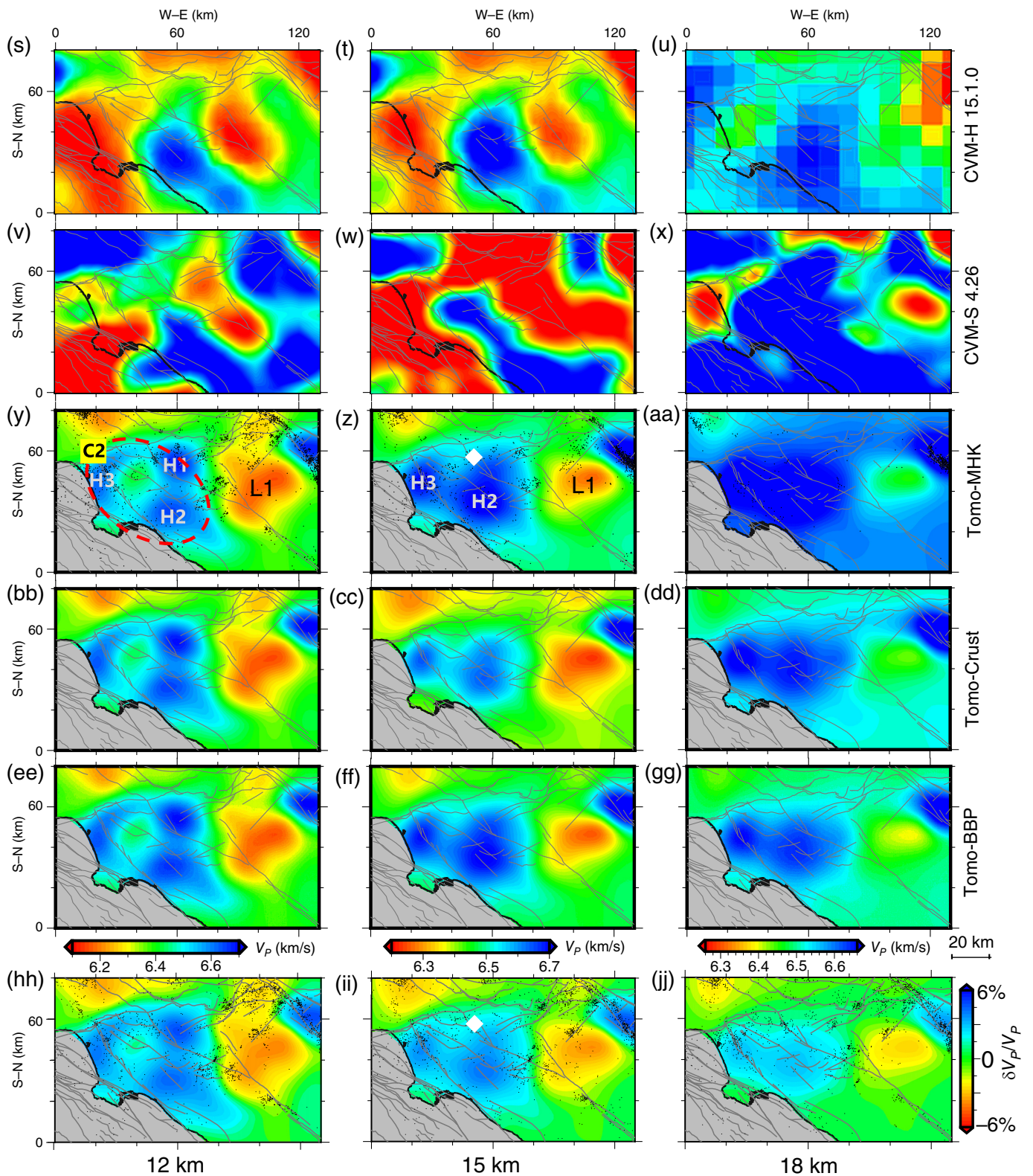
Figure 3. Continued
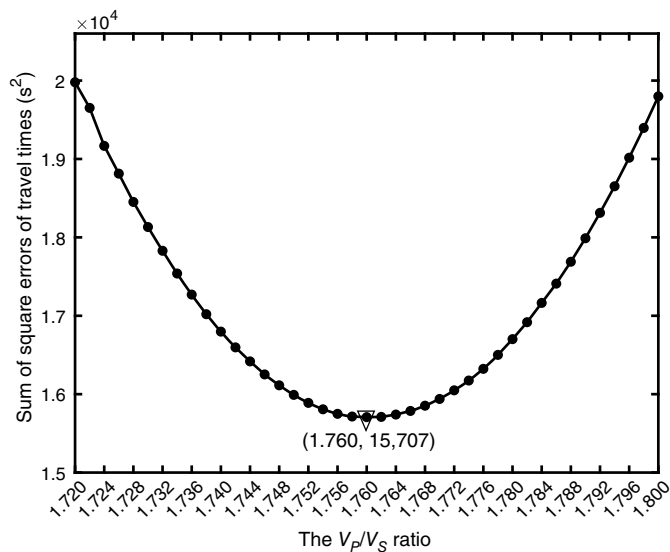
Figure 4. The sum of square errors of S-wave travel times in different V_S models. The V_S models are derived by dividing the V_P model by V_P/V_S ratios ranging from 1.720 to 1.780 at intervals of 0.002. The triangle indicates the minimum point on the curve.

tests (Fig. 2, Fig. S4). Because the model is best resolved for depths of less than 15 km, we do not place much emphasis on interpreting the models below this depth.

The LAB

In our velocity models, the area at 3 km depth within the LAB exhibits large-scale low-V_P and low-V_S, with values less than 5.6 and 3.0 km/s, respectively, associated with the Holocene–Upper Cretaceous sedimentary rocks (Reding, 1991; Süss and Shaw, 2003). Based on the depth extent of the low-V_P anomalies, similar to previous studies (e.g., Chen et al., 2007), we estimate the maximum depth of the LAB to be ~10 km (Figs. 3, 7c–e, 8c, and 9a). According to Fuis et al. (2001), areas with high-V_P (higher than 6.1 km/s) and high-V_P anomalies (higher than 2%) are considered to be occupied by basement rocks (Figs. 3p–r,hh–jj and 8c). Large-scale high-V_P/V_S ratios, higher than 1.82, are observed within the basin, extending from shallow depths to ~18 km depth (Figs. 6r and 9c).

The thickness of the low-V_P anomalies (less than −3%) shown in Figure 3 exhibits variations within the LAB, being shallower in the west of the Newport–Inglewood fault, and

the northwest, north, and east of the basin compared to the central region (Figs. 3p–r and 7a–e). This pattern is consistent with the distribution of low-intensity residuals (Hauksson et al., 2008, fig. 10A). In the northern and southwestern parts of the basin, our model reveals evident boundaries between high- and low-V_P anomalies (Fig. 7c–e), which moderately to steeply dip into the central basin from 2 to 10 km. These V_P boundaries align well with the traces of faults in horizontal maps at shallow depth, such as the SMoF (Chen et al., 2007, fig. 14) (Fig. 3p), the Newport–Inglewood fault (Lee et al., 2014; Shaw et al., 2015) (Fig. 3p–r), and the Whittier fault (Lee et al., 2014) (Fig. 3p–r), which form the basin margin together (Shaw et al., 2015). These boundaries along the active faults suggest differences in rock properties across the fault zone, which may be a key factor influencing the stress accumulation, the seismogenic slip behavior, and the down-faulting of the LAB (Hauksson, 1987). Therefore, our velocity models not only highlight the velocity contrast along the active faults and basin margin but also provide valuable tools for studying the seismic activity of these active faults, assessing future earthquake risks, and even understanding the basin's historical evolution.

Basement rocks

Our velocity models beneath the PVH, SMM, SGM, and the northwestern part of PR show high-V_P (higher than 5.4 km/s) and high-V_S (greater than 3.0 km/s) at 3 km depth, similar to previously published models (e.g., Hauksson and Haase, 1997; Chen et al., 2007; Lee et al., 2014; Shaw et al., 2015). The high-V_P zone, enclosed within the contour of 1.8% anomalies beneath the ranges, presents a vertically continuous feature extending from near the surface to the middle crust (Figs. 7a–e and 9b), forming the basement rocks beneath the LAB. In comparison with CVM-H 15.1.0 and CVM-S 4.26, our models show high-V_P (higher than 5.6 km/s) at 3 km depth (Fig. 3g,j,m) beneath both the west of the Newport–Inglewood fault and the PVH, whereas CVM-H 15.1.0 and CVM-S 4.26 display low to medium-V_P values (5.0–5.4 km/s) in these areas. We suspect that the high-V_P rocks in our models may reveal the joint uplift of basement rocks in both the PVH and the region west of the Newport–Inglewood fault.

The basement rocks of the northern PR Province are described within the framework of two Miocene and older structural blocks: the eastern and western LAB (Yerkes and

TABLE 2
Root Mean Square (rms), Calculated from Five Different V_P Models, Measure the Difference Between Synthetic and Observed Travel Times

Model	CVM-H 15.1	CVM-S 4.26	MHK	Crust	BBP
rms (s)	0.477878	0.670215	0.240747	0.240991	0.241365

The seismic data used in forward calculating are the remaining 46,974 P-wave seismic travel times after screening in the Data section. See the second paragraph of V_P model section for a discussion of how these rms values were calculated. CVM-H 15.1, Community Velocity Model-Harvard 15.1; CVM-S 4.26, Community Velocity Model Southern California Earthquake Center 4.26; and MHK, modified Hadley–Kanamori.
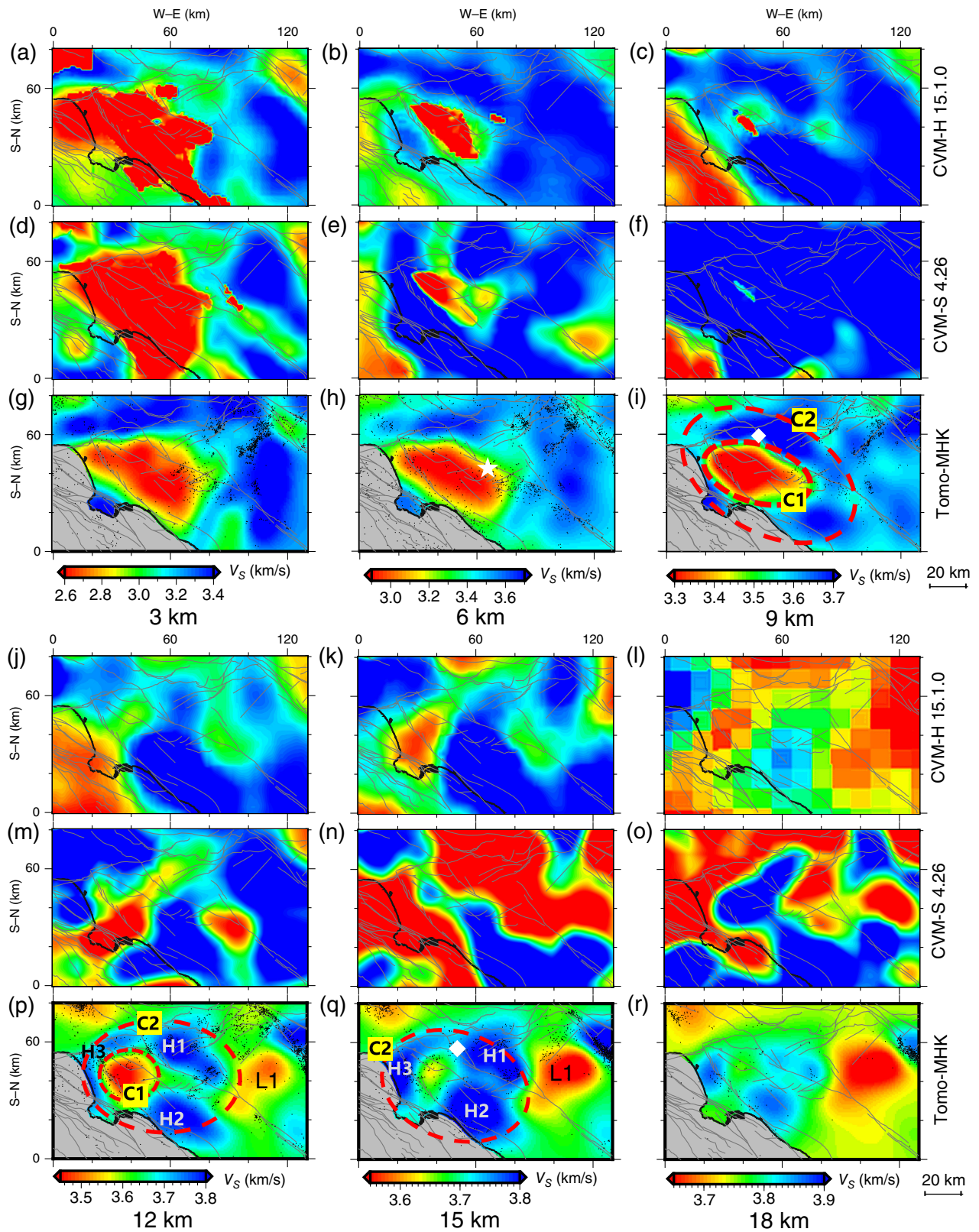
Figure 5. Comparison of V_S models in map views among (a–c, j–l) CVM-H 15.1 (Shaw *et al.*, 2015), (d–f, m–o) CVM-S 4.26 (Lee *et al.*, 2014), and (g–i, p–r) the model generated in this study. The color scale at each depth is included at the bottom. Other settings are the same as in Figure 3. The color version of this figure is available only in the electronic edition.
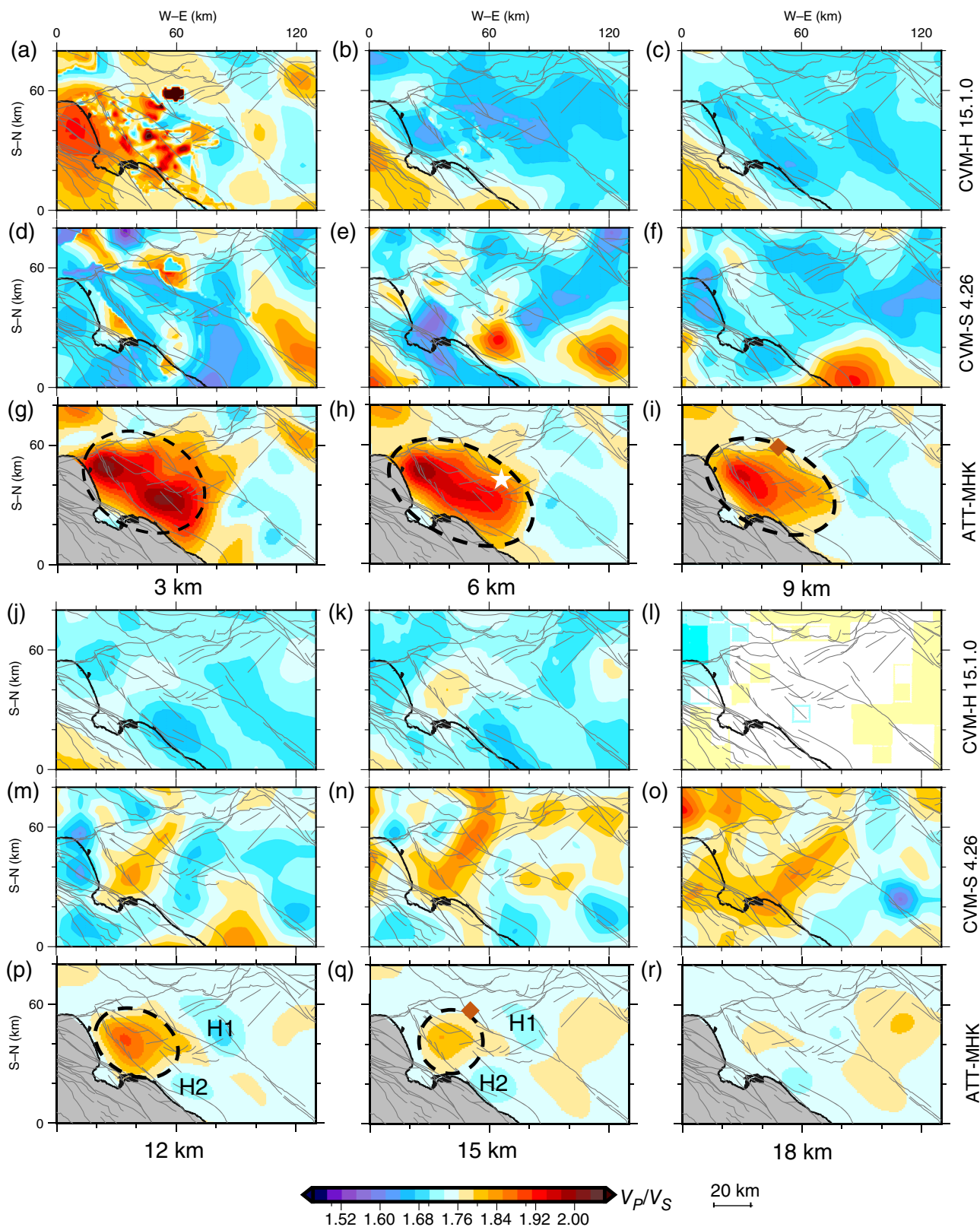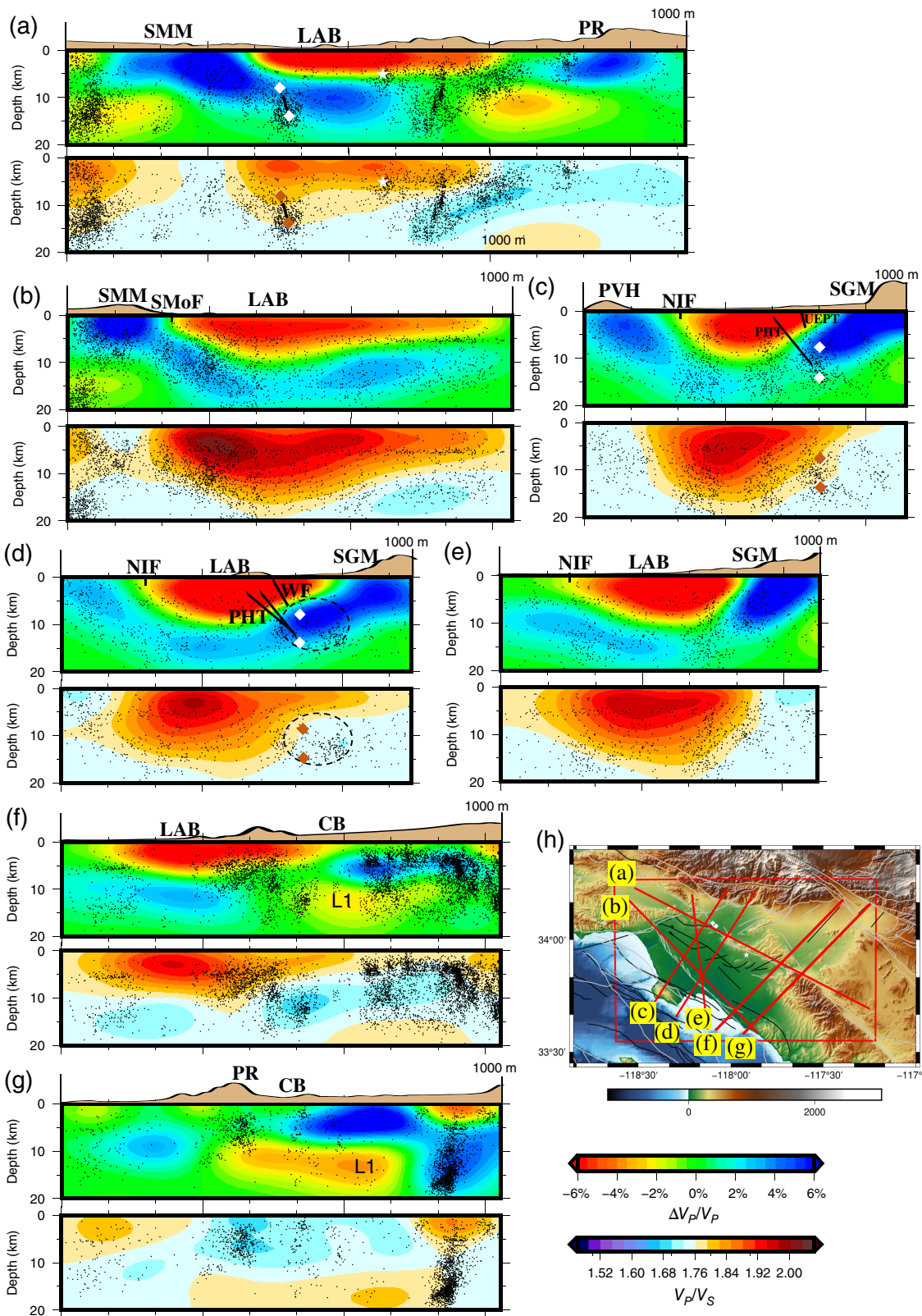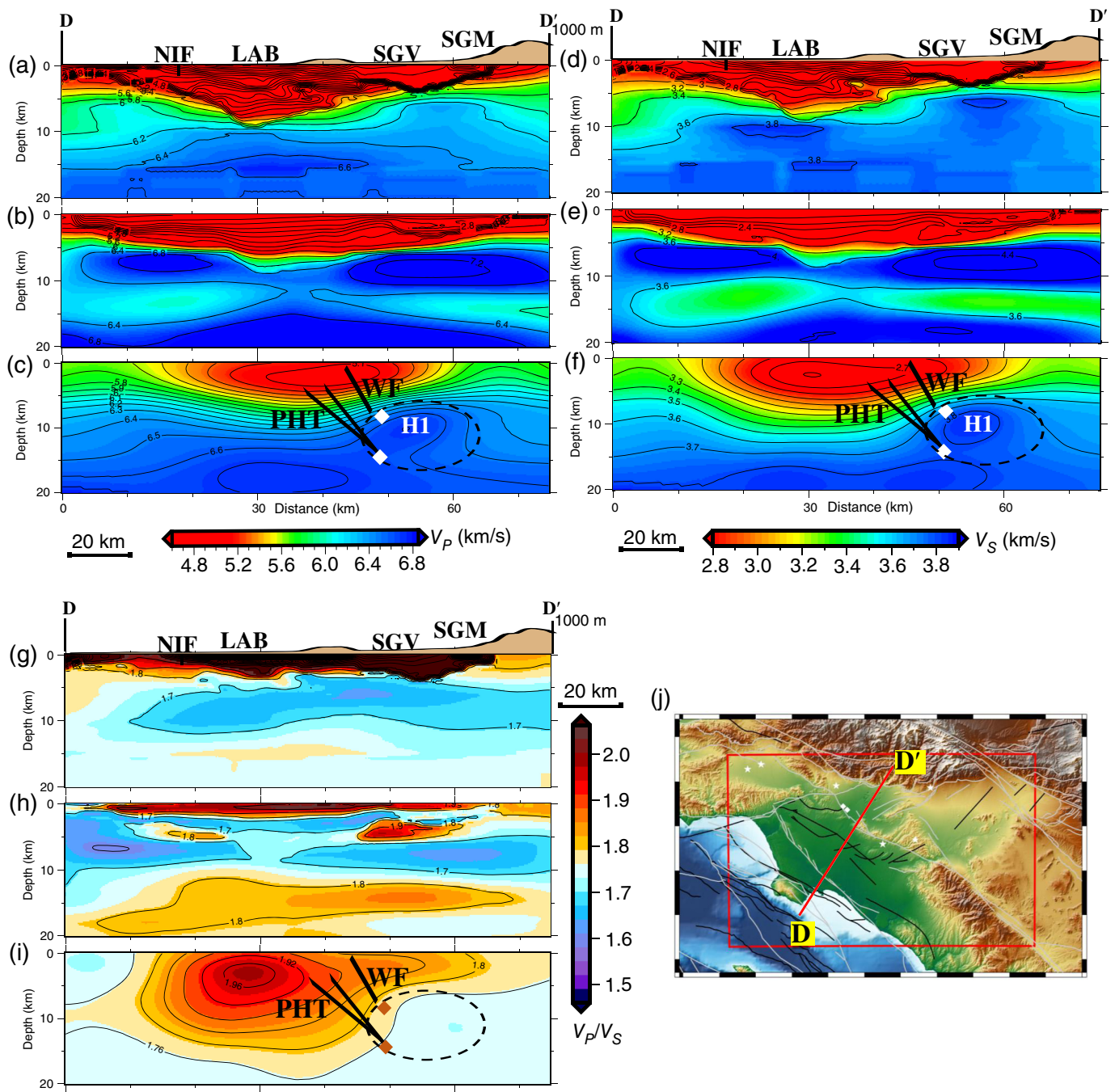
Figure 6. Comparison of V_P/V_S models in map views among (a–c,j–l) CVM-H 15.1.0 (Shaw *et al.*, 2015), (d–f,m–o) CVM-S 4.26 (Lee *et al.*, 2014), and (g–i,p–r) the model generated in this study. The color scale for V_P/V_S is included at the bottom. Other settings are the same as in Figure 3. The color version of this figure is available only in the electronic edition.

Figure 7. (a–g) Cross-section views of the V_P and V_P/V_S model along seven profiles. (h) The locations of the seven profiles are displayed. The color scales for V_P perturbation and V_P/V_S are shown at the bottom of the profiles. The black dots in perturbation profiles denote earthquakes that occurred within 5 km of the cross sections with a magnitude greater than 2.0. The diamonds represent the 1987 M_w 5.2 Whittier Narrows Aftershock and M_w 5.9 mainshock. The white star represents the 2014 M_w 5.2 La Habra earthquake. The black solid lines in panels (a), (c) and (d) roughly denote the projected shape of faults of PHT, WF, and UEPT (Plesch *et al.*, 2007, their fig. 7). All the abbreviations are the same as Figure 1a. The color version of this figure is available only in the electronic edition.

Figure 8. Cross-sectional comparison of (a–c) V_P, (d–f) V_S, and (g–i) V_P/V_S along profile D–D′ between CVM-H 15.1.0, CVM-S 4.26, and models obtained in this study. Profile location is shown in panel (j). Other settings are the same as those in Figure 7. The color version of this figure is available only in the electronic edition.

Campbell, 2005). In our velocity models, the high-V_P (6.4–6.7 km/s), high-V_S (3.6–3.8 km/s), and low-V_P/V_S (1.68–1.72), referred to as C2, H1, H2, and H3 in Figures 3, 5, 6, and 9d, respectively, suggest the northern extension of the PR batholith (Yerkes and Campbell, 2005). This extension clearly outlines the basement rocks surrounding the deep basin structure below 9 km depth (Figs. 3i,l,o,r,y,z,bb,cc,ee,ff,hh,ii and 5i,p,q). The area, marked as H3, may indicate the western block, whereas H1 and H2 correspond to the northeastern and southeastern blocks, respectively. However, in the CVM-H 15.1.0 and CVM-S 4.26 models, the western (H3) and northeastern (H1) basement rocks beneath the basin are not depicted below 9 km depth (Figs. 3c,f,s,v and 5c,f). In contrast, our velocity

models depict the structure of the basin's basement rocks, providing evidence that the LAB extends to about 10 km depth.

According to Magistrale and Zhou (1996), minerals in the schists become plastic at lower temperatures in southern California, suggesting that earthquakes occurring within schist basement rocks generally occur at shallower depths (4–10 km) compared to those occurring within other types of basement

Figure 9. 3D illustrations of (a) low-V_P anomalies, (b) high-V_P anomalies, (c) high-V_P/V_S structures, and (d) low-V_P/V_S structures. Vertical exaggeration of 3:1 is used. All symbols are explained similarly to those in Figure 1. The color version of this figure is available only in the electronic edition.
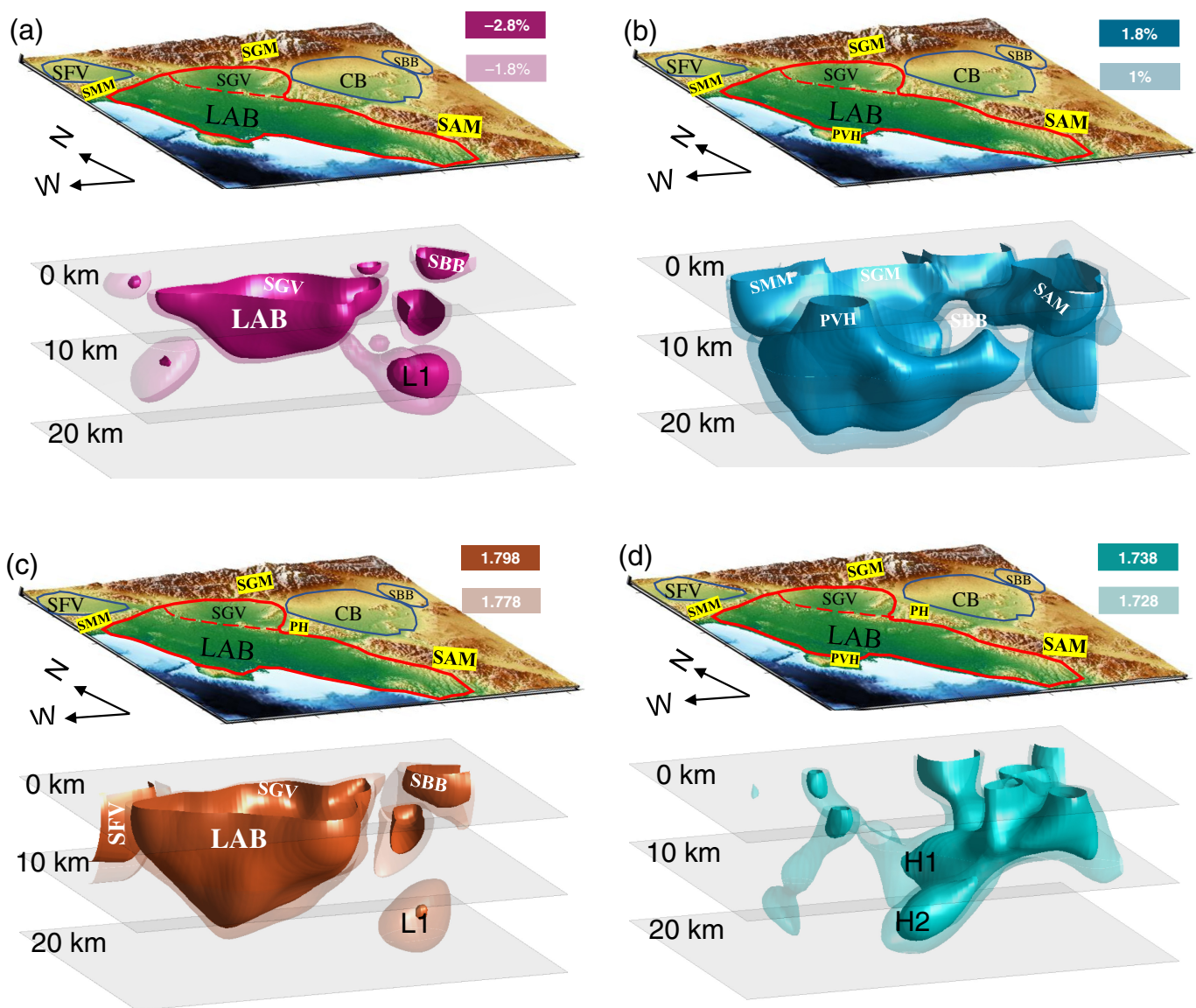
rocks. In our V_P model, the number of earthquakes (black dots) in H2 is generally fewer than in H1 and H3 from 9 to 15 km depth (Figs. 3i,r,y,z,hh,ii and 5i,p,q), consistent with the observation by Magistrale and Zhou (1996). This observation further implies that H2, the northernmost extension of the PR batholith, may contain Catalina and Pelona schist rocks (Hauksson and Haase, 1997).

Middle crust low-velocity anomaly

Beneath the eastern study region, including the CB and the northwestern part of the PR, the most prominent feature in the middle crust is the presence of a low-V_P (∼6.1–6.3 km/s) and low-V_S (lower than 3.6 km/s) anomaly, referred to as L1 (Figs. 3y,z, 5p–r, 7f,g, and 9a,c), with a maximum amplitude reaching −3%. This aligns with a low-V_P anomaly reported by Chen et al. (2007, their fig. 14), CVM-H 15.1.0 (Figs. 3s,t and 5j,k), CVM-S 4.26 (Figs. 3v,w and 5m,n), and Wu, Jiang, et al. (2022, their fig. 3; Wu, Li, et al., 2022, their fig. 4). In addition,

high-V_P/V_S ratios (>1.78) are detected at 15 km depth (Figs. 6q,r and 7f,g) within L1. In the map views (Fig. 3), the L1 region exhibits low-seismicity. The Moho depth beneath L1 is comparable to that of the western/central Mojave to the north (Li et al., 2021). Based on these observations, we speculate that the area with low-velocity anomaly referred to as L1 may have a structure similar to the complex crustal schists beneath the western/central Mojave Desert (Miller et al., 2000; Wu, Li, et al., 2022).

The 2014 M_w 5.1 La Habra earthquake

In the northern LAB, earthquakes are associated with active east–west-trending blind thrusts, such as the Puente Hills

Thrust and the upper Elysian Park Thrust (Hauksson *et al.*, 1988; Shaw *et al.*, 2002; Plesch *et al.*, 2007). For example, the focal mechanism of the 2014 M_w 5.1 La Habra earthquake (the star in Figs. 3h,q, 5h, and 6h) is related to the Puente Hills Thrust (Donnellan *et al.*, 2014). Near the La Habra earthquake hypocenter, our seismic velocity models show high-V_P/V_S ratios (about 1.88 in Figs. 6h and 7a), low V_P (about 5.8 km/s in Fig. 3h,q), and low-V_S (about 2.94 km/s in Fig. 5h). The V_P and V_S values near the La Habra earthquake are similar to those in CVM-H 15.1.0 and CVM-S 4.26 (Figs. 3b,e and 5e), whereas our V_P/V_S ratio is higher than that in CVM-H 15.1.0 (about 1.67) and CVM-S 4.26 (about 1.82).

According to Poisson's ratio as a function of V_P for common lithologies (Brocher, 2005, his fig. 3), our models suggest that the La Habra earthquake may have ruptured sedimentary rocks (Johnson and Christensen, 1992). Similar to the interpretation of the 1995 M_w 7.2 Kobe earthquake in Japan (Zhao *et al.*, 1996), the 1992 M_w 7.3 Landers earthquake (Fialko, 2004), and the 2019 M_w 7.1 Ridgecrest earthquake (Tong *et al.*, 2021), we speculate that the over-pressurized, fluid-filled, and fractured sedimentary rocks near the Puente Hills Thrust may have contributed to the initiation of the 2014 M_w 5.1 La Habra earthquake.

Comparison to previous models

One of the most prominent differences between the CVM-H 15.1.0, CVM-S 4.26, and the velocity models obtained in this study is highlighted in Figures 3 and 5 by a dashed circle at 9 km depth (C1). C1 has a low-V_P (less than −3% or below 6.0 km/s), low-V_S (less than 3.4 km/s) anomaly surrounded by a high-V_P (higher than 3% or 6.35–6.70 km/s), high-V_S (3.65–3.80 km/s) anomaly. In contrast, at a depth of 9 km, CVM-S 4.26 shows only high-V_P (higher than 6.4 km/s) and high-V_S (higher than 3.7 km/s) structures, whereas CVM-H 15.1.0 exhibits an area of low to medium-V_P (below 6.2 km/s) beneath the center of the LAB. Similar differences are observable at 12 km depth as highlighted by C2 (Figs. 3i,y and 5i,p,q). These differences suggest that the basin sedimentary rocks and basement structures of the LAB in our models are different from those in CVM-H 15.1.0 and CVM-S 4.26.

Basin effects have been demonstrated to significantly prolong shaking durations. One of the suggested reasons for this extended shaking is the conversion of body waves to surface waves at the edges of the basin (Joyner, 2000; Claire and Igor, 2003). Our models reveal distinct basin margins and a deep basin shape, potentially reflecting conditions conducive to prolonged seismic durations.

Figure 8 shows that the three models display similar patterns of velocity heterogeneity. For example, both the LAB and the SGV exhibit low-V_P (less than 5.4 km/s) and low-V_S (less than 3.1 km/s). However, several differences should be noted. First, the resolution of a velocity model is primarily determined by the data used in the tomographic inversion. Our

velocity models are determined by fitting the extensive amount of first travel-time data collected over the past four decades in the Los Angeles region. Therefore, the resolution is influenced by the spatial distribution of seismic stations within the regional seismic network and the distribution of seismicity. Because of the fact that seismic stations are spaced at an average minimum distance of greater than 3.5 km, our dataset has limited resolution for very shallow structures, specifically the first 1–2 km in depth (Fig. S4e). Other community velocity models, which incorporate seismic first travel-time data from dense arrays or industrial applications, offer higher resolution at shallow depths (Fig. 8a,b,d,e,g,h). Specifically, CVM-H 15.1.0 integrates multiple datasets, including borehole observations, seismic reflection, and refraction surveys, and earthquake body- and surface-wave data (Shaw *et al.*, 2015). CVM-S 4.26 incorporates earthquake seismograms and ambient-noise correlograms, which provide dense and uniform coverage throughout the entire modeling domain (Lee *et al.*, 2014, their fig. 1). However, our model has the best performance in fitting the regional seismic first travel-time data.

Second, the shape of the high-velocity area marked by the dashed circle in Figure 8, also referred to as H1 in Figures 3 and 5, is consistent with CVM-H 15.1.0, showing a similar protruding shape beneath the SGV. In contrast, CVM-S 4.26 shows this region as a relatively flattened high-V_S body (3.6–4.4 km/s). Specifically, the area beneath the SGV, indicated by the dashed circle in Figure 8c,f, exhibits high-V_P (6.3–6.8 km/s), high-V_S (3.5–3.8 km/s), and a medium-V_P/V_S ratio (~1.76). According to the empirical relationships for common lithologies described by Brocher (2005, table 2, figs. 2 and 3), this area may consist of metagreywackes and mafic rocks (Brocher and Christensen, 2001), which is consistent with the interpretation by Fuis *et al.* (2001), who also reported V_P values ranging from 6.3 to 6.8 km/s. In addition, near the aftershocks of the Whittier Narrows earthquake, within the dashed circle in Figure 8 and indicated by the diamond in Figures 3i, 5i, 6i, and 8c,f, the area is associated with the Puente Hills Thrust (Fuis *et al.*, 2001; Shaw *et al.*, 2002). Our seismic models for this region show high-V_P (6.47 km/s in Fig. 3i), high-V_S (3.60 km/s in Fig. 5i), and a high-V_P/V_S ratio (about 1.80 in Fig. 6i). In comparison, the V_P (V_S) values near the aftershocks in CVM-H 15.1.0 and CVM-S 4.26 are about 6.10 (3.65) km/s and 7.10 (4.25) km/s, respectively. Using the "mafic line" (Brocher, 2005, his equation 8) as the empirical relation between V_P and V_S, the differences between the calculated and inverted V_S values are 0.328, 0.408, and 0.086 km/s in CVM-H 15.1.0, CVM-S 4.26, and our model, respectively. This indicates that our tomographic models for H1 more accurately adhere to the "mafic line" relationship, perhaps suggesting the accuracy and reliability of the V_S model obtained in the present study.

The differences discussed in this section are likely caused by using different types of seismic data, physical models for modeling seismic wave propagation, and inversion strategies in

constructing the various velocity models. We emphasize the differences among these models and recommend a detailed investigation into the causes. The main purpose of our study is to construct seismic velocity models that can effectively explain the massive amount of first travel-time data accumulated in the past 40 yr. As shown in Table 2, our V_P models demonstrate the best performance in fitting first travel-time data alone. The differences highlighted by C1 and C2 in Figures 3 and 5 suggest notable variations in the distribution of basin sedimentary rocks and basement rocks among the velocity models. Accurately delineating the basin's structure, including the well-constrained western (H3), southeastern (H2), and northeastern (H1) basement rocks, the 10 km thickness of sedimentary rocks, and the distinct basin margin along active faults, is crucial for effective seismic hazard assessment. The 3D V_P anomalies provide a clear view of the basin's subsurface structure and its basement, revealing a distinct western basin basement (Fig. 9b) and a well-defined western basin margin along the Newport–Inglewood fault (Fig. 9a). In addition, our V_P and V_S models demonstrate greater accuracy and reliability in constraining the northeastern basement (H1), validated by the "mafic line" (Brocher, 2005, his equation 8), thus improving our understanding of the basement mafic rocks. Consequently, the well-defined velocity models developed in this study provide useful constraints for seismic response modeling and seismic hazard assessment.

CONCLUSIONS

In our study, we utilize the ATT method to generate high-resolution crustal velocity models with a grid size of 0.25 km × 0.25 km × 0.4 km. These models can reliably resolve horizontal structures at scales of 20 km and vertical structures at scales of 5 km beneath the LAB and its eastern adjacent region. 151,193 first P-wave travel times and 149,997 first S-wave travel times from local earthquakes are carefully selected and inverted, with earthquake locations updated at every iteration.

The obtained tomographic models effectively fit the extensive database of the first P and S arrival times accumulated over the past 40 yr within errors of measurement. Because the average spacing of seismic stations is more than 3.5 km apart, our dataset has limited resolution in the uppermost 1–2 km. However, starting from different initial models, our three V_P models, optimally imaged at depths between 3 and 15 km, exhibit similar velocity heterogeneity and a better fit to the observed first P-wave travel-time data compared to the CVM-H 15.1.0 and CVM-S 4.26 models. In addition, the velocity models show greater accuracy and reliability compared to both CVM-H 15.1.0 and CVM-S 4.26 in the northern basement of the LAB (H1). This is supported by the "mafic line" (Brocher, 2005), which provides evidence for improved constraints on basement mafic rocks in our models.

Our velocity models not only highlight the velocity contrast along the active faults and basin margin but also image the northeastern (H1) and western (H3) basement rocks. The observed differences, such as the low-velocity anomaly encircled by C1 and the high-velocity structures H1–H3 (C2), indicate variations in the distribution of the basin's deep sedimentary rocks and basement rocks among the velocity models, which requires further investigation into the causes of these discrepancies.

Accurate delineation of the basin's structure, highlighting the western (H3) and northeastern (H1) basement rocks, the 10 km thickness of sedimentary rocks, and the distinct basin margin along the active faults based on our models, is crucial for effective seismic hazard assessment. In summary, the well-defined velocity models developed in this study not only offer strong constraints for seismic response modeling but also provide useful tools for seismic hazard assessment.

DATA AND RESOURCES

DECLARATION OF COMPETING INTERESTS

The authors acknowledge that there are no conflicts of interest recorded.

ACKNOWLEDGMENTS

REFERENCES

Bjorklund, T., K. Burke, H. W. Zhou, and R. S. Yeats (2002). Miocene rifting in the Los Angeles basin: Evidence from the Puente Hills half-graben, volcanic rocks, and *P*-wave tomography, *Geology* **30,** 451–454.

Brocher, T. M. (2005). Empirical relations between elastic wave speeds and density in the Earth's crust, *Bull. Seismol. Soc. Am.* **95,** 2081–2092.

Brocher, T. M., and N. I. Christensen (2001). Density and velocity relationships for digital sonic and density logs from coastal Washington and laboratory measurements of Olympic Peninsula mafic rocks and greywackes, *U.S. Geol. Surv. 2001-264,* 39 pp.

Chen, P., L. Zhao, and T. H. Jordan (2007). Full 3D tomography for the crustal structure of the Los Angeles region, *Bull. Seismol. Soc. Am.* **97,** 1094–1120.

Claire, E. H., and A. B Igor (2003). Empirical corrections for basin effects in stochastic ground-motion prediction, based on the Los Angeles basin analysis, *Bull. Seismol. Soc. Am.* **93,** 1679–1690.

Crouch, J. K., and J. Suppe (1993). Late Cenozoic tectonic evolution of the Los Angeles basin and inner California borderland: A model for core complex-like crustal extension, *Geol. Soc. Am. Bull.* **105,** 1415–1434.

Davis, P. M., J. L. Rubinstein, K. H. Liu, S. S. Gao, and L. F. Knopoff (2000). Northridge earthquake damage caused by geologic focusing of seismic waves, *Science* **289,** 1746–1750.

Davis, T., J. S. Namson, and R. F. Yerkes (1989). A cross section of the Los Angeles area: Seismically active fold and thrust belt, The 1987 Whittier Narrows earthquake, and earthquake hazard, *J. Geophys. Res.* **94,** 9644–9664.

Donnellan, A., J. Parker, L. G. Ludwig, and E. Hauksson (2014). Activation of fault structures south of the La Habra earthquake rupture as evidenced by UAVSAR imaging, *Eos. Trans. AGU,* San Franciso, 15–19 December 2014 (Fall Meet.), S21B-4435.

Fialko, Y. (2004). Evidence of fluid-filled upper crust from observations of postseismic deformation due to the 1992 M_w 7.3 Landers earthquake, *J. Geophys. Res.* **109,** no. B8, doi: 10.1029/2004JB002985.

Fuis, G. S., T. Ryberg, N. J. Godfrey, D.A. Okaya, and J. M. Murphy (2001). Crustal structure and tectonics from the Los Angeles basin to the Mojave Desert, southern California, *Geology* **29,** 15–18.

Gao, S., H. Liu, P. M. Davis, and L. Knopoff (1996). Localized amplification of seismic waves and correlation with damage due to the Northridge earthquake: Evidence for focusing in Santa Monica, *Bull. Seismol. Soc. Am.* **86,** S209–S230.

Ghose, R., P. Persaud, and R. W. Clayton (2023). Basin structure for earthquake ground motion estimates in urban Los Angeles mapped with nodal receiver functions, *Geoscience* **13,** 320, doi: 10.3390/geosciences13110320.

Graves, R. W., and A. Pitarka (2010). Broadband ground-motion simulation using a hybrid approach, *Bull. Seismol. Soc. Am.* **100,** 2095–2123.

Graves, R. W., A. Pitarka, and P. G. Somerville (1998). Ground-motion amplification in the Santa Monica area: Effects of shallow basin-edge structure, *Bull. Seismol. Soc. Am.* **88,** 1224–1242.

Hauksson, E. (1987). Seismotectonics of the Newport-Inglewood fault zone in the Los Angeles basin, southern California, *Bull. Seismol. Soc. Am.* **77,** 539–561.

Hauksson, E. (2000). Crustal structure and seismicity distribution adjacent to the Pacific and North America plate boundary in southern California, *J. Geophys. Res.* **105,** 13,875–13,903.

Hauksson, E., and J. S. Haase (1997). Three-dimensional V_P and V_P/V_S velocity models of the Los Angeles basin and central Transverse Ranges, California, *J. Geophys. Res.* **102,** 5423–5453.

Hauksson, E., K. Felzer, D. Given, M. Giveon, S. Hough, K. Hutton, H. Kanamori, V. Sevilgen, S. Wei, and A. Yong (2008). Preliminary report on the 29 July 2008 M_w 5.4 Chino Hills, eastern Los Angeles basin, California, earthquake sequence, *Seismol. Res. Lett.* **79,** 855–866.

Hauksson, E., L. M. Jones, T. L. Davis, L. K. Hutton, P. Williams, A. L. Bent, A. G. Brady, P. A. Reasenberg, A. J. Michael, R. F. Yerkes, *et al.* (1988). The 1987 Whittier narrows earthquake in the Los Angeles metropolitan area, California, *Science* **239,** 1409–1412.

Hauksson, E., W. Yang, and P. M. Shearer (2012). Waveform relocated earthquake catalog for southern California (1981 to June 2011), *Bull. Seismol. Soc. Am.* **102,** 2239–2244.

Hutton, K., J. Woessner, and E. Hauksson (2010). Earthquake monitoring in southern California for seventy-seven years (1932-2008), *Bull. Seismol. Soc. Am.* **100,** 423–446.

Ingersoll, R. V., and P. E. Rumelhart (1999). Three-stage evolution of the Los Angeles basin, southern California, *Geology* **27,** 593–596.

Jia, Z., and R. W. Clayton (2021). Determination of near surface shear-wave velocities in the central Los Angeles basin with dense arrays, *J. Geophys. Res.* **126,** e2020JB021369, doi: 10.1029/2020JB021369.

Johnson, J. E., and N. I. Christensen (1992). Shear wave reflectivity, anisotropies, Poisson's ratios, and densities of a southern Appalachian Paleozoic sedimentary sequence, *Tectonophysics* **210,** 1–20.

Joyner, W. B. (2000). Strong motion from surface waves in deep sedimentary basins, *Bull. Seismol. Soc. Am.* **90,** S95–S112.

Laske, G., G. Masters, Z. Ma, and M. E. Pasyanos (2013). Update on CRUST1.0—A 1-degree Global Model of Earth's Crust, *EGU General Assembly Conference Abstracts*, Vienna, Austria, 7–12 April 2013, EGU2013-2658.

Lee, E., P. Chen, T. H. Jordan, P. Maechling, M. A. Denolle, and G. C. Beroza (2014). Full-3D tomography for crustal structure in southern California based on the scattering-integral and the adjoint-wavefield methods, *J. Geophys. Res.* **119,** 6421–6451.

Leung, S., and J. Qian (2006). An adjoint state method for three-dimensional transmission travel-time tomography using first-arrivals, *Comm. Math. Sci.* **4,** 249–266.

Li, T., J. Yao, S. Wu, and P. Tong (2021). Moho complexity in southern California revealed by local *PmP* and teleseismic *PS*-waves, *J. Geophys. Res.* **127,** doi: 10.1029/2021JB023033.

Li, Y., V. Villa, R. W. Clayton, and P. Persaud (2023). Shear wave velocities in the San Gabriel and San Bernardino basins, California. *J. Geophys. Res.* **128,** e2023JB026488, doi: 10.1029/2023JB026488.

Liu, G., P. Persaud, and R. W. Clayton (2018). Structure of the northern Los Angeles basins revealed in teleseismic receiver functions from short-term nodal seismic arrays, *Seismol. Res. Lett.* **89,** 1680–1689.

Liu, X., G. C. Beroza, L. Yang, and W. L. Ellsworth (2021). Ambient noise Love wave attenuation tomography for the LASSIE array across the Los Angeles basin, *Sci. Adv.* **7,** 1–6.

Magistrale, H., and H. Zhou (1996). Lithologic control of the depth of earthquakes in southern California, *Science* **273,** 639–642.

Magistrale, H., K. L. Mclaughlin, and S. M. Day (1996). A geology-based 3D velocity model of the Los Angeles basin sediments, *Bull. Seismol. Soc. Am.* **86,** 1161–1166.

Marshall, S., A. Plesch, and J. Shaw (2023). *SCEC Community Fault Model (CFM) (6.1)*, [Data set], doi: 10.5281/zenodo.8327463.

Miller, J. S., A. F. Glazner, G. L. Farmer, I. B. Suayah, and L. A. Keith (2000). A Sr, Nd, and Pb isotopic study of mantle domains and crustal structure from Miocene volcanic rocks in the Mojave Desert, California, *GSA Bull.* **112,** 1264–1279.

Muir, J., R. W. Clayton, V. C. Tsai, and Q. Brissaud (2021). Parsimonious velocity inversion applied to the Los Angeles basin, CA, *J. Geophys. Res.* **127,** no. 2, 1–20.

Nardoni, C., and P. Persaud (2024). Evidence for faulting and fluid-driven earthquake processes from seismic attenuation variations beneath Los Angeles, *Sci. Rep.* **14,** 17595, doi: 10.1038/s41598-024-67872-3.

Olsen, K. B., R. J. Archuleta, and J. R. Matarese (1995). Three-dimensional simulation of a magnitude 7.75 earthquake on the San Andreas fault, *Science* **270,** 1628–1632.

Persaud, P., Y. Ma, J. M. Stock, J. A. Hole, G. S. Fuis, and L. Han (2016). Fault zone characteristics and basin complexity in the southern Salton trough, California, *Geology* **44,** 747–750.

Plesch, A., J. H. Shaw, C. Benson, W. A. Bryant, S. Carena, M. L. Cooke, J. F. Dolan, G. S. Fuis, E. M. Gath, L. B. Grant, *et al.* (2007). Community Fault Model (CFM) for southern California, *Bull. Seismol. Soc. Am.* **97,** 1793–1802.

Qi, Y., and P. Tong (2022). Structure of the crustal magmatic system in the Geysers-Clear Lake area (northern California) imaged by adjoint-state travel-time tomography, *Seismol. Res. Lett.* **94,** 414–427.

Qiu, H., F. Lin, and Y. Ben-Zion (2019). Eikonal tomography of the southern California plate boundary region, *J. Geophys. Res.* **124,** 9755–9779.

Reding, T. W. (1991). Oil and gas production from submarine fans of the Los Angeles basin, in *Active Margin Basins*, K. T. Biddle (Editor), Vol. 52, American Association of Petroleum Geologists, Tulsa, Oklahoma, 5–24.

Shaw, J. H., A. Plesch, J. F. Dolan, T. L. Pratt, and P. Fiore (2002). Puente Hills blind-thrust system, Los Angeles, California, *Bull. Seismol. Soc. Am.* **92,** 2946–2960.

Shaw, J. H., A. Plesch, C. Tape, M. P. Suess, T. H. Jordan, G. Ely, E. Hauksson, J. Tromp, T. Tanimoto, R. W. Graves, *et al.* (2015). Unified structural representation of the southern California crust and upper mantle, *Earth. Planet. Sci. Lett.* **415,** 1–15.

Small, P. E., P. J. Maechling, and M. H. Su (2022). The Unified Community Velocity Model (UCVM) (22.7.0), *Zenodo* doi: 10.5281/zenodo.7033687.

Southern California Earthquake Center (SCEDC) (2013). *Southern California Earthquake Center* [Dataset], Caltech, Pasadena, California, doi: 10.7909/C3WD3xH1.

Steidl, J. H., L. F. Bonilla, and A. G. Tumarkin (1995). Site effect study in the San Fernando basin, Los Angeles, California: A comparison of methods (abstract), *Eos Trans. AGU* (Fall Meet., Suppl. 76), 351 pp.

Süss, M. P., and J. H. Shaw (2003). *P*-wave seismic velocity structure derived from sonic logs and industry reflection data in the Los Angeles basin, California, *J. Geophys. Res.* **108,** 2170, doi: 10.1029/2001JB001628.

Tape, C., Q. Liu, A. Maggi, and J. Tromp (2009). Adjoint tomography of the southern California Crust, *Science* **325,** 988–992.

Tong, P. (2021). Adjoint-state travel-time tomography: Eikonal equation-based methods and application to the Anza area in southern California, *J. Geophys. Res.* **126,** e2021JB021818, doi: 10.1029/2021JB021818.

Tong, P., D. Yang, and X. Huang (2019). Multiple-grid model parameterization for seismic tomography with application to the San Jacinto fault zone, *Geophys. J. Int.* **218,** 200–223.

Tong, P., J. Yao, Q. Liu, T. Li, K. Wang, S. Liu, Y. Cheng, and S. Wu (2021). Crustal rotation and fluids: Factors for the 2019 Ridgecrest earthquake sequence? *Geophys. Res. Lett.* **48,** 1–10.

Tsutsumi, H., R. S. Yeats, and G. J. Huftile (2001). Late Cenozoic tectonics of the northern Los Angeles fault system, California, *Geol. Soc. Am. Bull.* **113,** 454–468.

Villa, V., Y. Li, R. W. Clayton, and P. Persaud (2023). Three-dimensional basin depth map of the northern Los Angeles basins from gravity and seismic measurements, *J. Geophys. Res.* **128,** e2022JB025425, doi: 10.1029/2022JB025425.

Wang, X., Z. Zhan, M. Zhong, P. Persaud, and R. W. Clayton (2021). Urban basin structure imaging based on dense arrays and Bayesian array-based coherent receiver functions. *J. Geophys. Res.* **126,** e2021JB022279, doi: 10.1029/2021JB022279.

Wessel, P., and W. H. Smith (1995). New version of the generic mapping tools, *Eos Trans. AGU* **76,** 329–329.

Wright, T. L. (1991). Structural geology and tectonic evolution of the Los Angeles basin, California: Chapter 3: Part 1, in *Active Margin Basins*, K. T. Biddle (Editor), Vol. 52, American Association of Petroleum Geologists, Tulsa, Oklahoma, 35–79.

Wu, S., C. Jiang, V. Schulte-Pelkum, and P. Tong (2022). Complex patterns of past and ongoing crustal deformations in southern California revealed by seismic azimuthal anisotropy, *Geophys. Res. Lett.* **49,** e2022GL100233, doi: 10.1029/2022GL100233.

Wu, S., T. Li, D. Wang, and P. Tong (2022). Lower crust structures and dynamics of southern California revealed by first *P* and *PmP* travel-time data, *Tectonophysics* **830,** 229328.

Yerkes, R. F., and R. H. Campbell (2005). Preliminary geologic map of the Los Angeles 30′ × 60′ Quadrangle, southern California, detailed description of map units, version 1.0, *U.S. Geol. Surv. Open-File Rept. 2005-1019.*

Yerkes, R. F., T. H. McCulloh, J. E. Schoellhamer, and J. G. Vedder (1965). Geology of the Los Angeles basin, California: An introduction, *U.S. Geol. Surv. Profess. Pap. 420A,* 57 pp.

Zhao, D., H. Kanamori, H. Negishi, and D. Wiens (1996). Tomography of the source area of the 1995 Kobe earthquake: Evidence for fluids at the hypocenter? *Science* **274,** 1891–1894.

Zhao, H. (2004). A fast sweeping method for eikonal equations, *Math. Comput.* **74,** 603–627.